Basic chemistry of tetrachloroaurate ion and its hydrolytic species and its application to material chemistry

川本, 大?

Basic chemistry of tetrachloroaurate ion and its hydrolytic species and its application to material chemistry

By

DAISUKE KAWAMOTO

Department of Chemistry, Faculty of Sciences,

Graduate School of Kyushu University,

March 2015

Content

Chapter I

General introduction

I-1　Background of thesis

In order to reveal the mobility of trace metals, it is important to be understood the dissolved species and the precipitation and adsorption behaviors of them in environment. From previous studies, the dissolved species of gold were demonstrated under various condition. The mobilization and the transport processes of gold are associated with gold complexes. Various inorganic and organic ligands were known to be important in mobilizing gold in certain environments.　Under most conditions, the prevalent dissolved gold complex was suggested to be $[Au(OH) \cdot H_2O]^0$[1].　Near oxdizing sulfide minerals, complexes such as $[Au(HS)_2]^-$, $[AuHS \cdot H_2O]^0$[2] and $[Au(S_2O_3)_2]^{3-}$[3] may aid the mobility and the dispersion of gold.　At high Cl^- concentration that exist in many arid regions, gold may be mobilized as $[AuCl_2]^-$ or $[AuCl_4]^-$ which are stable under acidic, oxic and high Cl^- condition[4].　Other important forms of the mobile gold may include gold complexes with organic matter[5], cyanide[6] and elemental colloidal gold[7].　In particular $[AuCl_4]^-$ converts to four dissolved species through successive hydrolysis dependent on the pH.　Each hydrolysis reaction is following;

$$[AuCl_4]^- \ + \ OH^- \ \rightarrow \ [AuCl_3(OH)]^- \ + \ Cl^-$$

$$[AuCl_3(OH)]^- \ + \ OH^- \ \rightarrow \ [AuCl_2(OH)_2]^- \ + \ Cl^-$$

$$[AuCl_2(OH)_2]^- \ + \ OH^- \ \rightarrow \ [AuCl(OH)_3]^- \ + \ Cl^-$$

$$[AuCl(OH)_3]^- \ + \ OH^- \ \rightarrow \ [Au(OH)_4]^- \ + \ Cl^-$$
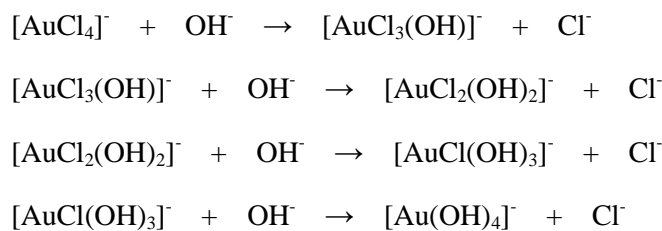
Figure I-1 shows the distribution curve of hydrolytic species for $[AuCl_4]^-$ in supergene waters ($Cl^- \ = \ 0.001$ mol/dm^3).　There are five hydrolytic species as $[AuCl_{4-n}(OH)_n]^-$ (n = 0-4). However, there is no detailed information on the change in their property associated with hydrolysis reaction.　In order to reveal the mobilization and transport process of gold, it is necessary to understand the differences of the properties between $[AuCl_4]^-$ and its four

hydrolytic species (i.e. electronic state).

On the other hand, in recent years, gold was used on the industrial fields as catalysts and gold alloy. Haruta et al. reported that gold nanoparticles supported metal oxide is useful as heterogeneous catalyst for the oxidation of carbon monoxide[8]. The supported gold catalyst was prepared by using gold (III) hydroxide as the precursor[9, 10], which is one of the hydrolytic product of $[AuCl_4]^-$ as shown Fig. I-2. However, the basic property of the gold (III) hydroxide has not been made clear. Even now, it is debated about the chemical composition and the chemical and physical properties. It is essential to reveal the basic properties of the gold (III) hydroxide in order to prepare the supported gold catalysts with high activity. Gold has been also used as gold alloy due to high corrosion resistance, ductility and high conductivity. In the metallurgical method which is a typical alloy preparation method, alloy is formed by melting the component elements. In this metallurgical method, there are three main problems: (1) a temperature above the melting point of the elemental metal component is necessary, (2) alloy with the desired composition is difficult to prepare if the optimum condition is impossible to attain, and (3) it is difficult to mold fine structures due to the different cooling conditions of liquid alloy with high temperature. Recently, an alloy preparation method using a chemical reaction has been studied because fine powder alloys can be obtained at lower temperature than the metallurgical method. However, it is difficult to obtain the alloy consisting of a single phase in the conventional methods such as chemical reaction. Therefore, a new preparation method of the alloy consisting of a single phase has been studied.

I-2   Purpose of thesis

As described in the above section, there are no detailed information on both the change in their property associated with hydrolysis reaction of $[AuCl_4]^-$, and the basic properties of gold (III) hydroxide.   Therefore, the purposes of this thesis were to elucidate the basic properties of both the hydrolytic species as $[AuCl_{4-n}(OH)_n]^-$ and gold (III) hydroxide, and to develop of the novel preparation method for powder alloys consisting of a single phase and the desired composition at low temperature.

This thesis consists of five chapters.

Chapter I describes a general introduction to the previous research and purposes of this investigation.

Chapter II describes the investigation of the change in electronic state associated with the successive hydrolysis of tetrachloroaurate ion ($[AuCl_4]^-$) using a relativistic version of the discrete variational (DV) $X\alpha$ method which is a first principle molecular orbital (MO) calculation method.

Chapter III describes identification of gold (III) hydroxide and its chemical and physical properties.

Chapter IV describes a novel and new preparation method for a single phase Au-Cu powder alloy and its characterization.

Chapter V describes the main results and conclusions of this thesis.

The basic properties of both the hydrolytic species as $[AuCl_{4-n}(OH)_n]^-$ and gold (III) hydroxide, and the novel preparation method for powder alloys in this thesis are very important to understand geochemistry of gold and to develop new gold materials.
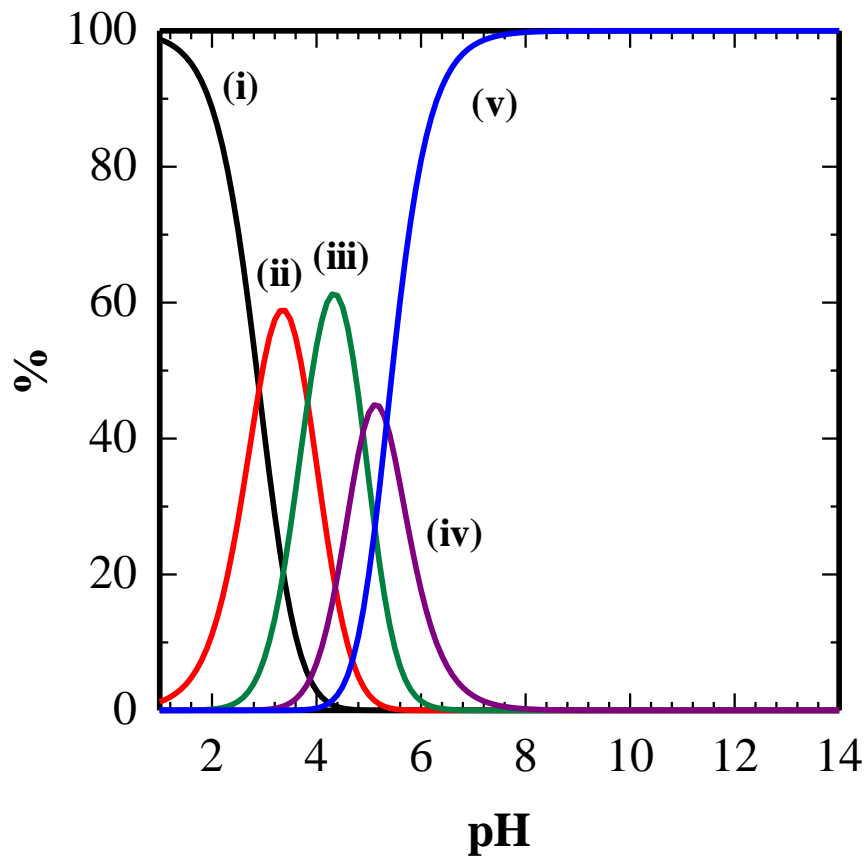
Fig. I-1   Distribution curve of hydrolytic species ($[AuCl_{4-n}(OH)_n]^-$)

in supergene waters ($Cl^- = 0.001$ mol/dm^3).

Each solid lines indicated $[AuCl_4]^-$ (i), $[AuCl_3(OH)]^-$ (ii),

$[AuCl_2(OH)_2]^-$ (iii), $[AuCl(OH)_3]^-$ (iv) and $[Au(OH)_4]^-$ (v).
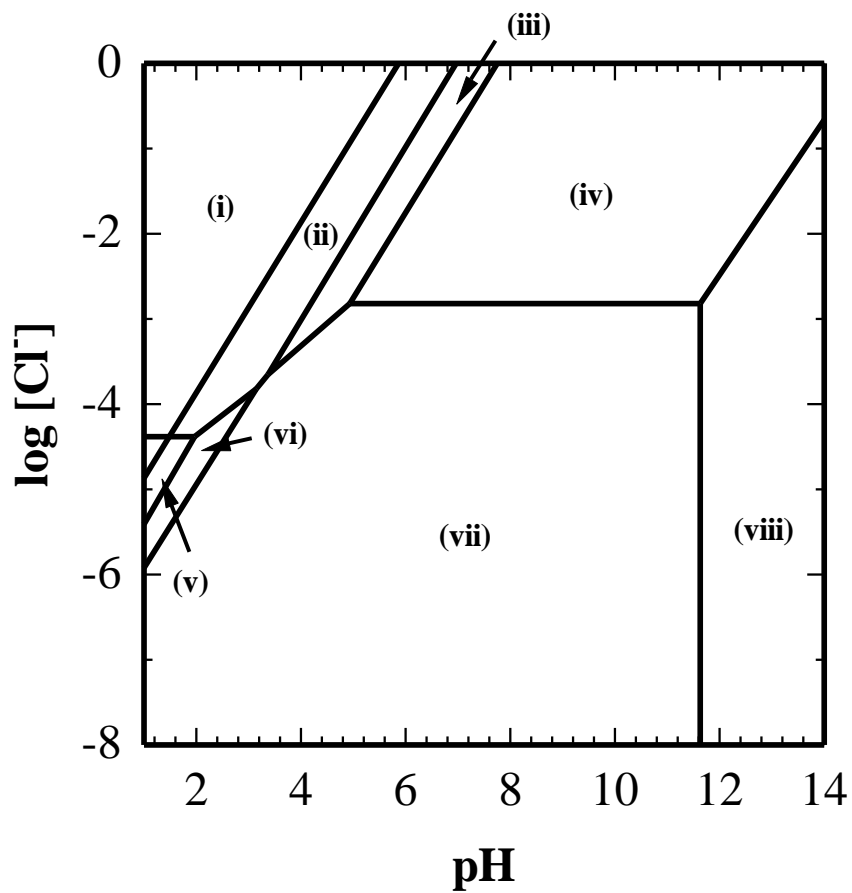
Fig. I-2　Predominance diagram of $[AuCl_{4-n}(OH)_n]^-$ and $AuCl_{3-m}(OH)_m$ (s) species (s : solid).

Each region indicated $[AuCl_4]^-$ (i), $[AuCl_3(OH)]^-$ (ii), $[AuCl_2(OH)_2]^-$ (iii), $[AuCl(OH)_3]^-$ (iv),

$AuCl_2(OH)$ (s) (v), $AuCl(OH)_2$ (s) (vi), $Au(OH)_3$ (s) (vii) and $[Au(OH)_4]^-$ (viii).

Chapter II

Change in electronic state of tetrachloroaurate ion in solution by its hydrolysis

II-1   Introduction

Hydrogen tetrachloroaurate $H[AuCl_4]$ is a representative reagent among gold (III) complexes.   The $[AuCl_4]^-$ hydrolyzes to form $[AuCl_{4-n}(OH)_n]^-$ (n = 0-4) step by step depending on pH and Cl^- concentration (Fig. II-1).   Although gold is classified into a group with moderate hardness based on the Hard and Soft Acids and Bases (HSAB) theory, it can easily combine with OH group which is hard base.   The stepwise hydrolysis reaction has been investigated by absorption spectrophotometry and Raman spectroscopy[11, 12].   The hydrolysis reaction is important in various fields.

In geochemistry in hydrosphere, gold is transported under high Cl^- concentration that exist in many arid regions.   Gold may be mobilized as $[AuCl_4]^-$ which is stable under acidic, oxic and high Cl^- conditions[4].   On the other hand, the mobility of gold is restricted by adsorption on the surface of various minerals. $[AuCl_4]^-$ which is stable under acidic condition is not adsorbed on the surface of metal (hydr)oxide and aluminosilicate minerals which are widely distributed in hydrosphere.   However, adsorption of gold proceeds with increasing pH in the range from weak acid to weak alkaline condition[13, 14].   The accelerated adsorption of gold is considered to depend on the hydrolysis of $[AuCl_4]^-$, that is, the amount of gold adsorbed increases along the distribution curve of $[AuCl_3(OH)]^-$, as shown in Fig. II-1.   The fact suggests that the adsorption may occur due to condensation reaction between OH groups of $[AuCl_{4-n}(OH)_n]^-$ and surface OH groups on the minerals to form metal-O-Au bond.

In the catalyst field, $H[AuCl_4]$ has been used to the preparation of the precursor for the supported gold catalyst.   The mixed solution of metal nitrate and $H[AuCl_4]$ is often added into

Na$_2$CO$_3$ solution to precipitate the precursor of supported gold catalyst. In this preparation method, the detailed coprecipitation mechanism of gold species with metal hydroxide cannot be understood due to complexity. Consequently, the hydrolysis of [AuCl$_4$]$^-$ has never been considered in the preparation.

As described above, the hydrolysis of [AuCl$_4$]$^-$ (substitution reaction of Cl$^-$ with OH$^-$) is important to elucidate in various field. However, it is, even at present, impossible to say that the hydrolysis is understood from the experimental researches. Due to the background, a theoretical study was tried in this study about the hydrolysis reaction. The aim of this study is to investigate about the change in the properties, especially the electronic states, for all the [AuCl$_{4-n}$(OH)$_n$]$^-$ (n = 0–4) using the first principle MO calculation and the variation of "net charge" and "bond overlap population" for Au, Cl and O atoms with n was examined. The net charge and the bond overlap population are measures for ionic bond character and covalent bond character in the MO calculation method used in this study.

II-2 Measurement of Au L₃-edge XANES spectra and Computational method

II-2-1 Measurement of Au L₃-edge XANES spectra for [AuCl₄]⁻ and [Au(OH)₄]⁻

To estimate the validity of this first principle MO calculation, it was compared the Au L₃-edge XANES spectra and the calculated transition peaks for $[AuCl_4]^-$ and $[Au(OH)_4]^-$.

$[AuCl_4]^-$ and $[Au(OH)_4]^-$ were prepared by dissolving $HAuCl_4 \cdot 4H_2O$ into 0.1 mol/dm³ HCl solution and by dissolving $NaAuCl_4 \cdot 2H_2O$ into 0.1 mol/dm³ NaOH solution. The Au L₃-edge XANES spectra for both complex ions were measured by transmission mode at BL14B2 beamline of SPring-8 (8 GeV and 99.5 mA). This measurement was conducted at room temperature (RT). The spectra were analyzed using software (Athena of Ifeffit)[15].

II-2-2 Optimization of structure

The crystal structure of anhydrous potassium tetrachloroaurate (III), $K[AuCl_4]$, is summarized in Table II-1[16]. A structure model of $[AuCl_4]^-$ and its hydrolytic species, $[AuCl_{4-n}(OH)_n]^-$, were optimized by Density functional Theory (DFT) calculation (Fig. II-2). In the calculation, "-1" charge was given to the complex ion. "+3" charge was given to Au ion and "-1" charge was given to Cl and OH group. Moreover, the hydration effect and the relativistic effect were considered. The calculation level was B3LYP/6-31G*, where B3LYP refers to the applied exchange-correlation functional[17, 18] and 6-31G* is the standard split-valence basis set. The relative energies reported in the paper have been obtained at the same level of theory. The optimized structure parameters for each hydrolytic species are summarized in Table II-2~II-7.

II-2-3 Features of the relativistic DV-Xα method and calculation method

The first principle MO calculation were performed using the relativistic DV-*Xα* method

developed by Rosen et al.[19] and improved later by Adachi et al.[20]. A MO of molecule is represented by the linear combination of atomic orbital (LCAO) approximation. The one electron Schrödinger equation with a nonrelativistic approximation for the MO calculation is written as eqs. (1) and (2)

$$H\Psi = E\Psi \qquad (1)$$

$$H = -\frac{p^2}{2m} + V_{eff}(\boldsymbol{r}) \qquad (2)$$

where Ψ is the wave functions (the molecular orbitals), E is the electronic energy, H is the Hartree-Fock-Slater Hamiltonian operator and $-p^2/2m$ (p is the momentum operator) is the electronic kinetic energy. $V_{eff}(\boldsymbol{r})$ is the effective potential energy expressed as a function of the electronic position $\boldsymbol{r}$ as eq. (3)

$$V_{eff}(\boldsymbol{r}) = \sum \frac{-Z_N}{|\boldsymbol{r}-\boldsymbol{R}_N|} + \int \frac{\rho(\boldsymbol{r'})}{|\boldsymbol{r}-\boldsymbol{r'}|} d\boldsymbol{r'} + V_{ex}(\boldsymbol{r}) \qquad (3)$$

where Z_N is atomic number, $|\boldsymbol{r}\text{-}\boldsymbol{R}_N|$ expresses the distance between an electron, $|\boldsymbol{r}\text{-}\boldsymbol{r'}|$ expresses the distance between an electron and the other electron and a nucleus and ρ is the electronic density. The first term represents the Coulomb potentials from the nuclei and the second term is the Coulomb potential from the other electrons. For the exchange potential $V_{ex}(\boldsymbol{r})$, the DV-$X\alpha$ method use the $X\alpha$ potential proposed by Slater[21] which is expressed as the cube root of the electronic density as eq. (4)

$$V_{ex}(\boldsymbol{r}) = -3\alpha \left\{ \frac{3}{8\pi} \rho(\boldsymbol{r}) \right\}^{1/3} \qquad (4)$$

where α is a parameter and can be determined by setting the total energy obtained by the $X\alpha$ method to be equal to that obtained by the Hartree-Fock method. However, it was reported that errors in MO calculations are generally negligible when using $\alpha = 0.7$[22].

On the other hand, when an atomic number is large, it becomes impossible to disregard the relativistic effects in electronic kinetic energy because the speed of an electron is very fast around the deep core regions, approaching the speed of light. In such a case, it is calculable with sufficient accuracy by changing the Schrödinger equation to the Dirac equation. The Dirac-Fock-Slater Hamiltonian in this case is written as eq. (5)

$$H = c\tilde{\alpha}p + \tilde{\beta}mc^2 + V_{eff}(r) \qquad (5)$$

where $\tilde{\alpha}$ and $\tilde{\beta}$ are Dirac matrices, m is the electronic mass and c is the velocity of light. The relativistic effects, such as the spin-orbit interaction, are included in the Dirac matrices. For the DV-$X\alpha$ method, the Dirac equation can be directly calculated using the $X\alpha$ potential, and relativistic four-component MOs can be obtained under consideration of symmetry based on the group theory.

The $[AuCl_{4-n}(OH)_n]^-$ include gold which is a heavy element.　For heavy elements of which atomic numbers are larger than 50 such as Au, the relativistic effects are remarkable in the electronic structure and chemical bonding[23, 24].　Therefore, in this study, a relativistic version of DV-$X\alpha$ method was used.

The relativistic DV-$X\alpha$ calculations were conducted for the models shown in Fig. II-2 and Tables II-2~II-7.　In the calculation, basis sets used were from *1s* to *6s* orbital for Au, from *1s* to *3p* orbital for Cl, from *1s* to *2p* orbital for O and *1s* orbital for H.　Convergence point of self-consistent-field iterations for all models was set 0.001 electrons in difference of electron before and after the iterations.　The calculations were made for both the ground state and Slater's transition state.　The transition probabilities of electric dipole transitions were calculated using the obtained MOs.　The theoretical X-ray absorption spectra were obtained from broadening each peak by a Gaussian function with a 0.25 eV full width at half maximum.

II-3　Results and discussion

The observed Au L_3-edge XANES spectra for [Au(OH)$_4$]$^-$ (a) and [AuCl$_4$]$^-$ (c), and the calculated transition peaks for [Au(OH)$_4$]$^-$ (b) and [AuCl$_4$]$^-$ (d) are shown in Fig. II-3.　Their calculated transition peaks were in good agreement with the observed Au L_3-edge XANES spectra for each complex ions, suggesting that this calculation condition using the relativistic DV-$X\alpha$ method is valid.　Thus, all the hydrolytic species ([AuCl$_{4-n}$(OH)$_n$]$^-$) were calculated on the same condition described above.　Further, their net charges and their bond overlap populations were compared among them.

Figure II-4 shows the net charges for [AuCl$_{4-n}$(OH)$_n$]$^-$ (n = 0–4).　The net charge of Au (●) was increased from 0.16 to 0.99 as hydrolysis proceeds, suggesting that the ionic property of Au is increased.　Especially, when [AuCl$_4$]$^-$ transforms to [AuCl$_3$(OH)]$^-$, the change in the net charge was largest compared with other transformation.　Although the net charge of Cl (△) in the [AuCl$_3$(OH)]$^-$ showed obviously low value of -0.46, the other hydrolytic species showed almost constant value of -0.35.　Therefore, the above results suggest that the change in the electronic state for Au and Cl is largest when first one of Cl$^-$ was substituted to OH group.　On the other hand, the net charge of O (■) was almost constant (-0.85).　Allred and Rochow have evaluated the property of the bond between two atoms from the difference in electronegativity of each atom.　The bond is covalent bond polarized when this value (χ) is less than 1.7, and the bond is ionic bond when that is more than 1.7.　According to this law, the Au-Cl bond (χ=1.41) is covalent bond polarized, and the Au-O bond(χ=2.08) is ionic bond.　This result is consistent with the above law and indicates quantitatively the change in the property of the bond between two atoms.　Despite that the formal charges of Au, Cl and O (OH) are "+3", "-1" and "-2" ("-1"), respectively, the values of their net charges were different from their formal charges after the calculation.　This difference is due to Pauling's second law.

The bond overlap populations for [AuCl$_{4-n}$(OH)$_n$]$^-$ are shown in Fig. II-5.　The bond overlap population is the overlap of each atomic orbital involved in the bond.　From its value

the binding multiplicity can be inferred, that is, 0.7 corresponds to the single bond, from 0.7 to 1.1 double bond and from 1.1 to 1.4 triple bond.   The values of the bond overlap population for Au-Cl and Au-O interactions were below 0.5, suggesting that Au-Cl and Au-O interactions are single bond.   Further, the value of the bond overlap population for the Au-Cl interaction decreased from 0.43 to 0.41 as hydrolysis proceeds.   On the other hand, in Au-O interaction, the value increased from 0.24 to 0.32 as hydrolysis proceeds.   Moreover, the value of the bond overlap population for Au-O interaction was lower than that for the Au-Cl interaction, suggesting that the Au-Cl interaction has stronger covalent bond property than that for the Au-O interaction.   Based on HSAB theory, Au^{3+} cation is the acid with moderate hardness.   On the other hand, Cl^- anion is softer base than O^{2-} anion.   Therefore, Au^{3+} cation which is the acid with moderate hardness has stronger affinity to Cl^- anion rather than O^{2-} anion.   In conclusion, it can be deduced that Au^{3+} ion in $[AuCl_4]^-$ is acid with softer property.   However, the Au^{3+} ion may change to Au^{3+} ion with harder property when first one of Cl^- substituted with OH^- group. Consequently, the hardness of Au^{3+} ion may be changed by substitution reaction of ligand.
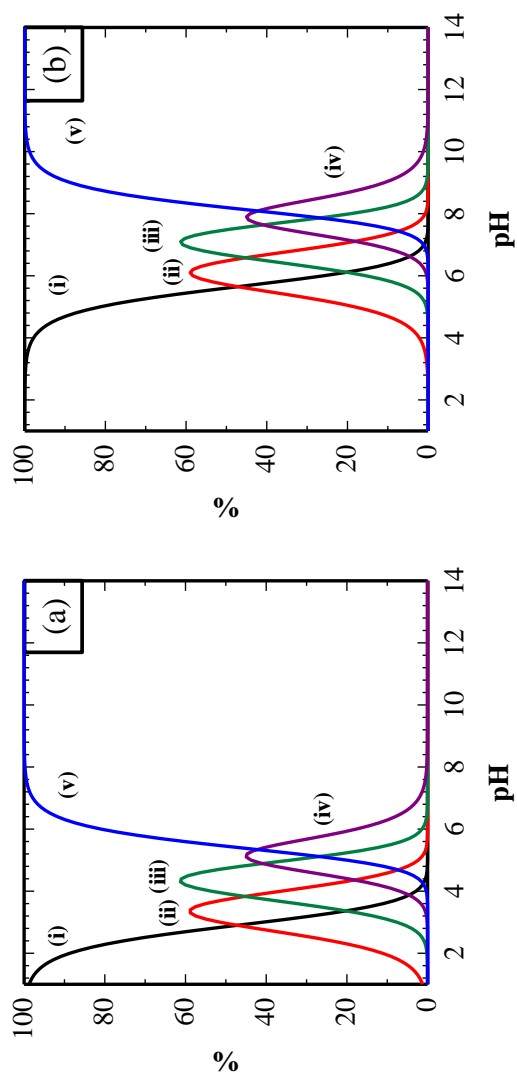
Fig. II-1   Distribution curve of hydrolytic species ($[AuCl_{4-n}(OH)_n]^-$)

in supergene waters ($Cl^- = 0.001$ mol/dm^3) (a) and in seawater ($Cl^- = 0.56$ mol/dm^3) (b).

Each solid lines indicated $[AuCl_4]^-$ (i), $[AuCl_3(OH)]^-$ (ii),

$[AuCl_2(OH)_2]^-$ (iii), $[AuCl(OH)_3]^-$ (iv) and $[Au(OH)_4]^-$ (v).

Table II-1   The crystal structure of anhydrous potassium tetrachloroaurate (III)[16].

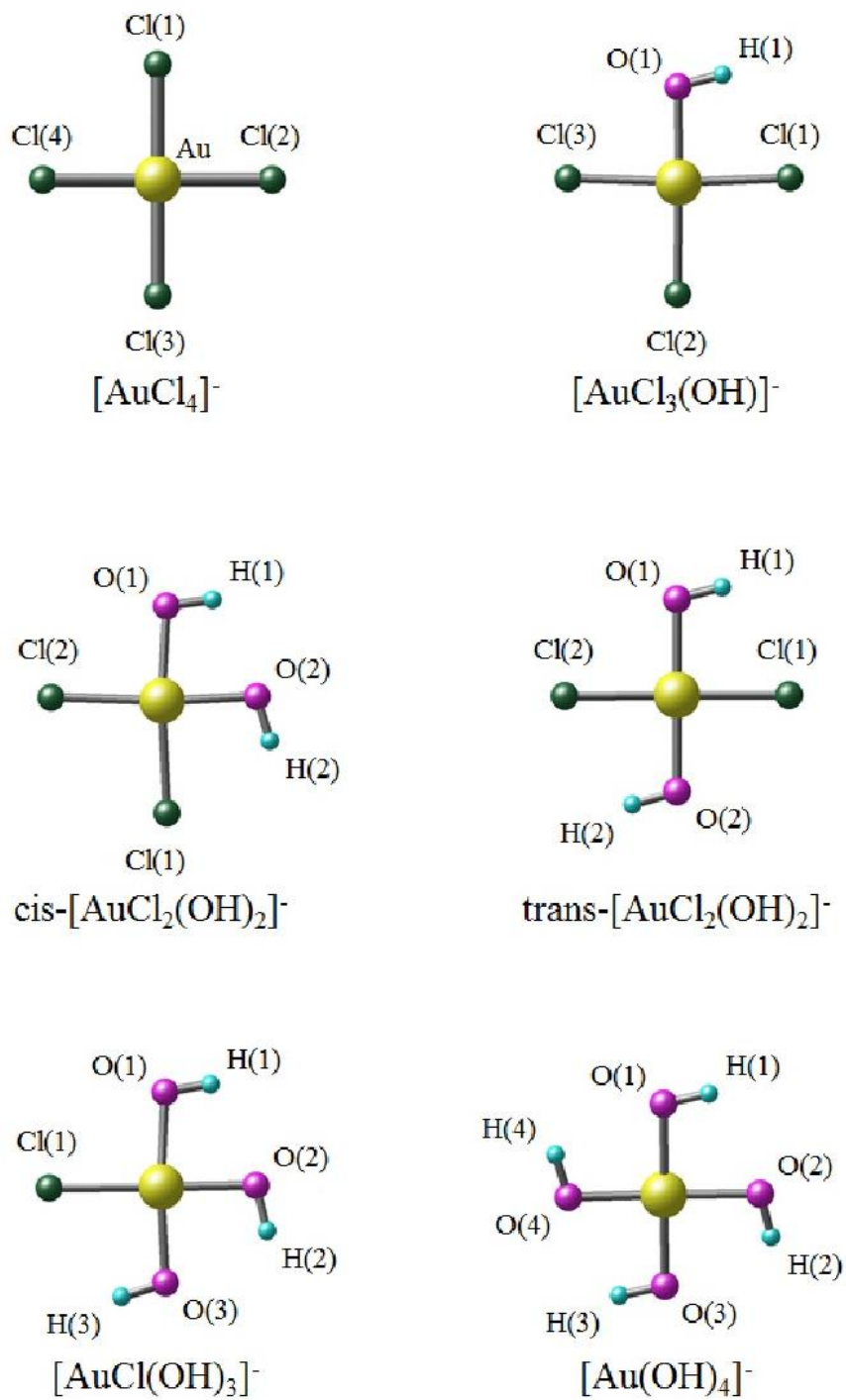|	Au-Cl bond length / Å	∠ClAuCl bond angle / °
K[AuCl$_4$]	2.26-2.29	89-90

Fig. II-2   The structure models of [AuCl$_4$]$^-$ and its hydrolytic species.

Table II-2　The optimized structure parameters for [AuCl$_4$]$^-$.

Bonds	Bond length / Å	Bond angles	Bond angle / °
Au-Cl(1)	2.42	∠Cl(1)AuCl(2)	90
Au-Cl(2)	2.42	∠Cl(2)AuCl(3)	90
Au-Cl(3)	2.42	∠Cl(3)AuCl(4)	90
Au-Cl(4)	2.42	∠Cl(4)AuCl(1)	90

Table II-3　The optimized structure parameters for [AuCl$_3$(OH)]$^-$.

Bonds	Bond length / Å	Bond angles	Bond angle / °
Au-Cl(1)	2.42	∠Cl(1)AuCl(2)	92.67
Au-Cl(2)	2.43	∠Cl(2)AuCl(3)	91.25
Au-Cl(3)	2.42	∠Cl(3)AuO(1)	87.73
Au-O(1)	2.06	∠O(1)AuCl(1)	88.35
O(1)-H(1)	1.01	∠AuO(1)H(1)	104.58

Table II-4　The optimized structure parameters for cis-[AuCl$_2$(OH)$_2$]$^-$.

Bonds	Bond length / Å	Bond angles	Bond angle / °
Au-Cl(1)	2.44	∠Cl(1)AuCl(2)	94.23
Au-Cl(2)	2.42	∠Cl(2)AuO(1)	90.76
Au-O(1)	2.05	∠O(1)AuO(2)	84.80
Au-O(2)	2.07	∠O(2)AuCl(1)	90.21
O(1)-H(1)	1.01	∠AuO(1)H(1)	100.78
O(2)-H(2)	1.00	∠AuO(2)H(2)	103.69

Table II-5　The optimized structure parameters for trans-[AuCl$_2$(OH)$_2$]$^-$.

Bonds	Bond length / Å	Bond angles	Bond angle / °
Au-Cl(1)	2.42	∠Cl(1)AuO(2)	90.15
Au-Cl(2)	2.42	∠Cl(2)AuO(1)	90.55
Au-O(1)	2.06	∠O(1)AuCl(1)	89.56
Au-O(2)	2.06	∠O(2)AuCl(2)	89.74
O(1)-H(1)	1.00	∠AuO(1)H(1)	105.08
O(2)-H(2)	1.00	∠AuO(2)H(2)	106.16

Table II-6　The optimized structure parameters for [AuCl(OH)$_3$]$^-$.

Bonds	Bond length / Å	Bond angles	Bond angle / °
Au-Cl(1)	2.44	∠Cl(1)AuO(1)	92.69
Au-O(1)	2.06	∠O(1)AuO(2)	86.75
Au-O(2)	2.06	∠O(2)AuO(3)	88.53
Au-O(3)	2.07	∠O(3)AuCl(1)	92.03
O(1)-H(1)	1.01	∠AuO(1)H(1)	101.79
O(2)-H(2)	1.01	∠AuO(2)H(2)	102.78
O(3)-H(3)	1.00	∠AuO(3)H(3)	105.51

Table II-7　The optimized structure parameters for [Au(OH)$_4$]$^-$.

Bonds	Bond length / Å	Bond angles	Bond angle / °
Au-O(1)	2.07	∠O(1)AuO(2)	89.73
Au-O(2)	2.07	∠O(2)AuO(3)	90.22
Au-O(3)	2.07	∠O(3)AuO(4)	88.90
Au-O(4)	2.07	∠O(4)AuO(1)	91.14
O(1)-H(1)	1.00	∠AuO(1)H(1)	102.98
O(2)-H(2)	1.00	∠AuO(2)H(2)	102.84
O(3)-H(3)	1.00	∠AuO(3)H(3)	102.38
O(4)-H(4)	1.00	∠AuO(4)H(4)	104.55
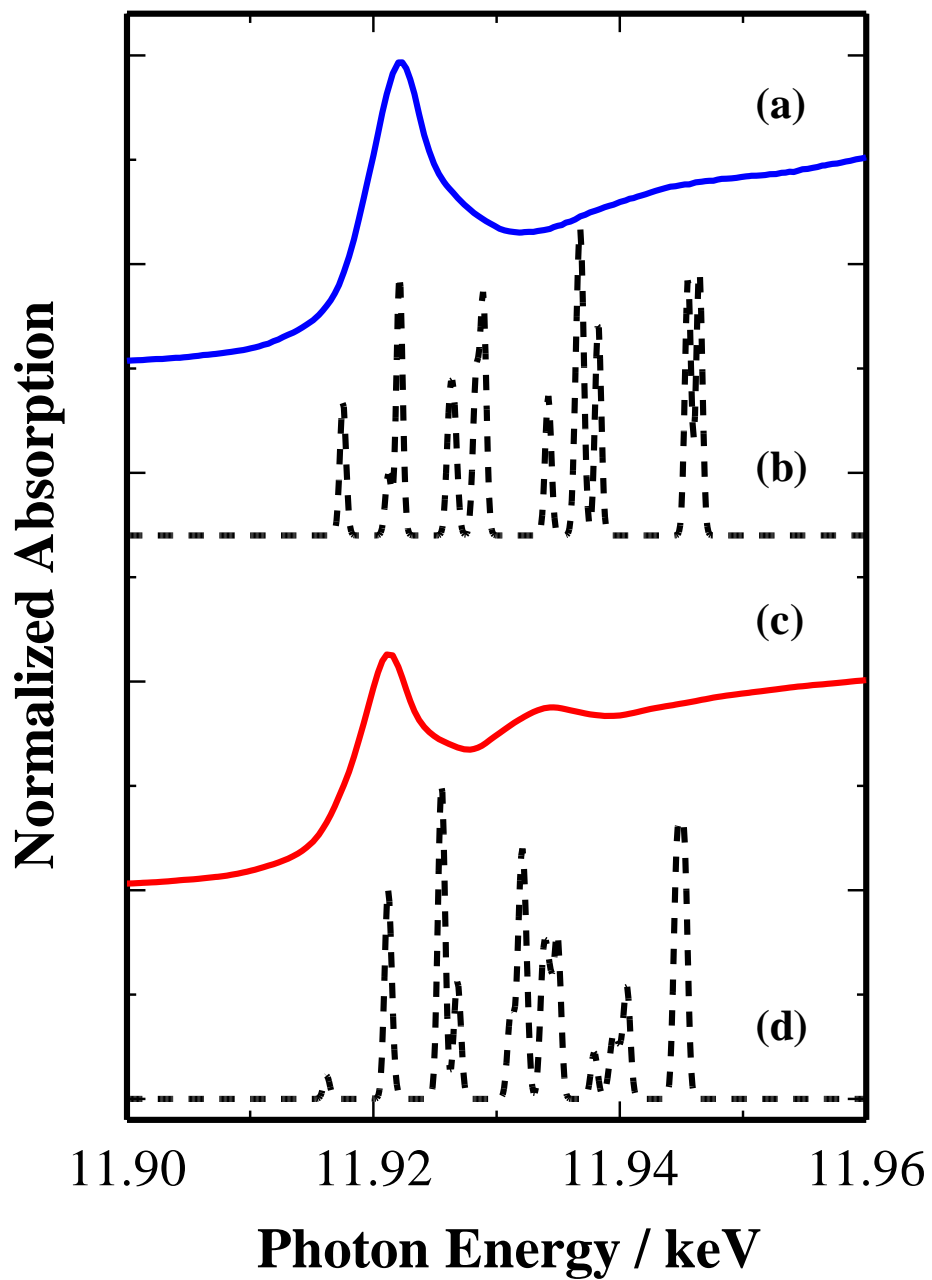
Fig. II-3 Normalized Au L$_3$-edge XANES spectra for [Au(OH)$_4$]$^-$ (a) and [AuCl$_4$]$^-$ (c),

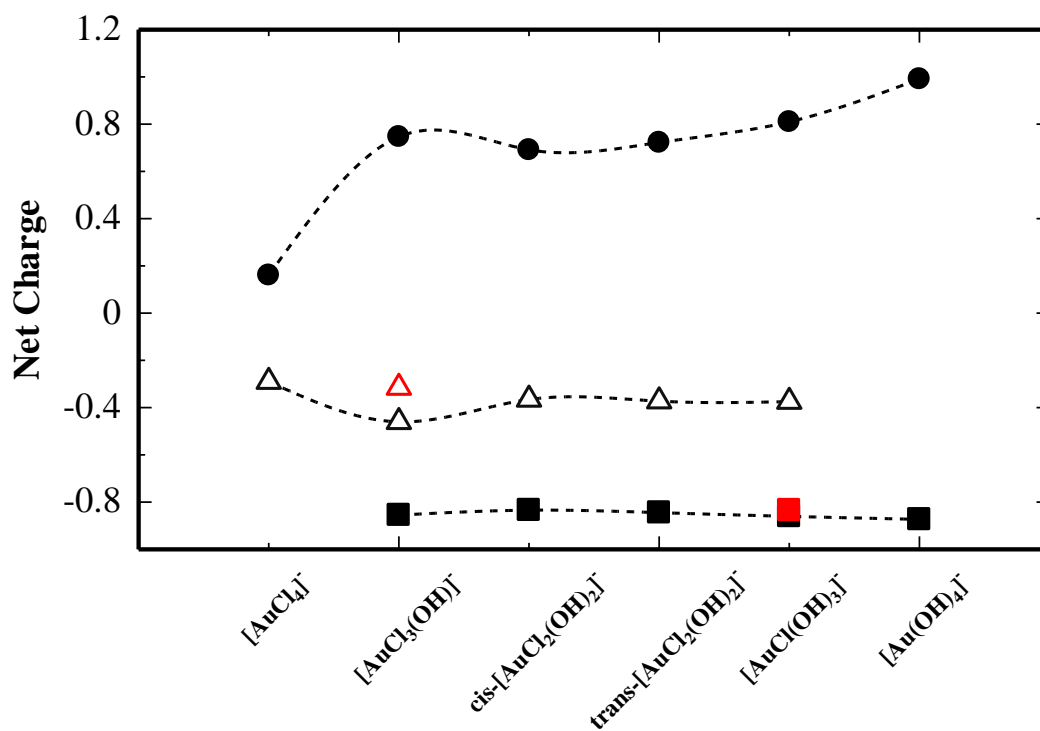and the calculated transition peaks for [Au(OH)$_4$]$^-$ (b) and [AuCl$_4$]$^-$ (d).

Fig. II-4   Net charges for $[AuCl_{4-n}(OH)_n]^-$ (n = 0-4).
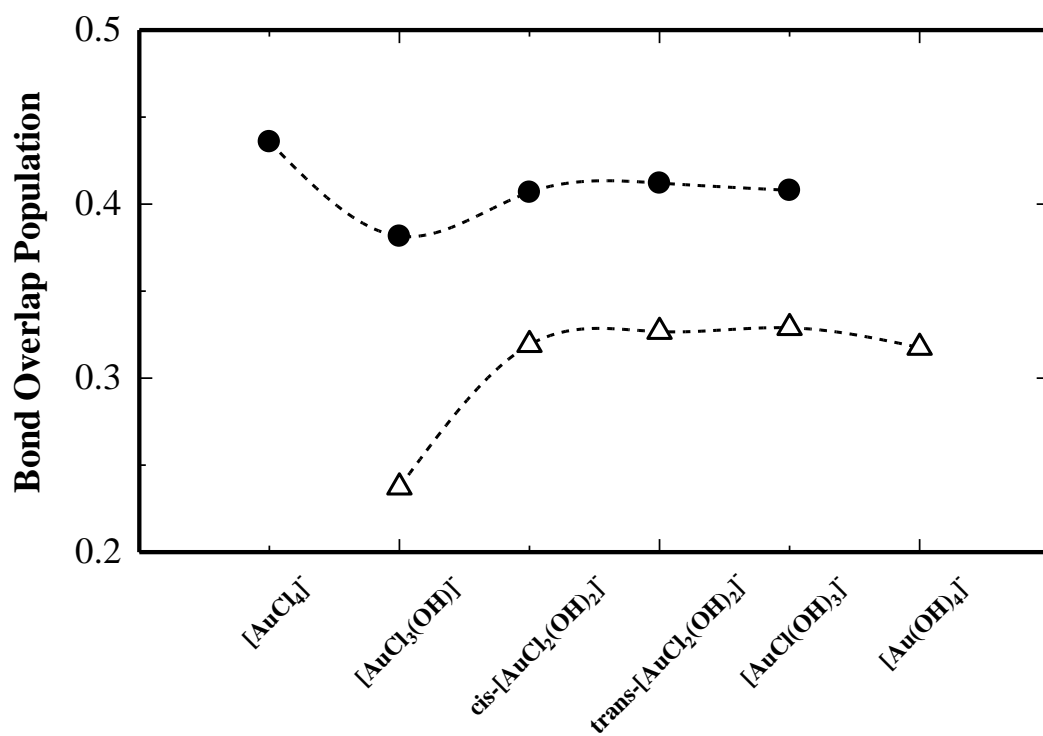
Their symbols indicate Au (●), Cl (△) and O (■).

Fig. II-5　Bond overlap populations for $[AuCl_{4-n}(OH)_n]^-$ (n = 0-4).

Their symbols indicate Au-Cl interaction (●) and Au-O interaction (△).

Chapter III

Identification of gold (III) hydroxide and its chemical and physical properties

III-1   Introduction

Gold has been used for currencies and ornament from ancient time because of universal value, that is, stability against oxidation.   In recent years, gold has been used on the industrial fields as gold alloy due to high corrosion resistance, specific ductility and high conductivity. Moreover, the gold nanoparticles and/or the gold alloy nanoparticles have been used as the catalyst [8, 25].   The precipitate in alkaline solution of $[AuCl_4]^-$, which has been believed to be gold (III) hydroxide, is used as the precursor to prepare these catalysts [10, 26].   However, whether the precipitate is gold (III) hydroxide ($Au(OH)_3$) or hydrous gold (III) oxide ($Au_2O_3 \cdot nH_2O$) have been uncertain even at present.   Although Herrick and Hollis tried to measure the solubility of the precipitate [27], no investigation on the chemical and physical properties has been performed.   The aim of this study is to examine about the chemical and physical properties of the precipitate through the characterization by X-ray powder diffraction (XRD), transmission electron microscopy (TEM), ^{197}Au Mössbauer spectroscopy, X-ray absorption spectroscopy (XAS), Thermogravimetry/Differential Thermal Analysis (TG/DTA), Attenuated Total Reflection-infrared spectroscopy (ATR-IR), Ultraviolet-Visible spectroscopy (UV-Vis), O_2-/H_2-Temperature Programmed Reaction (O_2-/H_2-TPR) and Solubility measurement.

Based on the results, I concluded finally that the precipitate is probably gold (III) hydroxide with a chemical composition of $Au(OH)_3$ although amorphous.   In addition, I tried to determine the solubility of $Au(OH)_3$.

III-2 Experimental

III-2-1 Chemicals

Reagents used in this study were of analytical reagent grade. Solutions were prepared with deionized-distilled water. $HAuCl_4 \cdot 4H_2O$ were purchased from TANAKA HOLDINGS Co., Ltd.. The gold (III) hydroxide was prepared based on the previous work[28].

III-2-2 Preparation of a precipitate from $HAuCl_4$ solution

Na_2CO_3 solution and $HAuCl_4$ solution were prepared by dissolving anhydrous Na_2CO_3 (4.9 g) into water (100 cm^3) and by dissolving $HAuCl_4 \cdot 4H_2O$ (4.0 g) into water (50 cm^3), respectively. The $HAuCl_4$ solution was mixed with the Na_2CO_3 solution and the mixed solution was magnetically stirred for 8 h. The obtained precipitate was filtered with 0.20 μm membrane filter, washed with water and then was freeze-dried under vacuum. Here, I call the precipitate "Au solid sample".

III-2-3 Characterization of the Au solid sample

XRD analysis of the Au solid sample was performed using Ultima IV (Rigaku) at a scanning rate of 2 °/min and at a step scan of 0.02 ° in 2θ range of 20-80 ° with Cu Kα radiation. The operating voltage and current were 40 kV and 30 mA, respectively.

The size and morphology of the Au solid sample were analyzed using HR TEM (JEOL ARM200F) operated at an acceleration voltage of 200 kV. TEM specimens were prepared by dispersing the Au solid sample into water. The suspended solution was put on a holey carbon mesh supported by a Cu grid and air-dried.

The ^{197}Au Mössbauer spectra were measured by transmission method at Research Reactor

Institute of Kyoto University.   The Au solid sample was placed in a Teflon sample holder. The spectra were measured at 9-12 K.   The γ-ray source (^{197}Pt) was prepared by neutron irradiation to ^{196}Pt (half-life: 18.6 h, γ-ray energy: 77.4 keV).   The spectra were analyzed using a computer software by assuming that each spectrum consists of Lorentzian function.

For the XAS measurement, the Au solid sample was diluted with boron nitride (BN) and the pellet was made.   The Au L$_3$-edge XAS was measured by transmission mode at BL14B2 beamline of SPring-8 (8 GeV and 99.5 mA).   This measurement was conducted at RT.   The spectra were analyzed using software (Athena and Artemis of Ifeffit) [15].   The curve fitting was carried out in R-space by Artemis with a Fourier transformed range of k = 3-12.5 Å^{-1} and a back-Fourier transform range of R = 1-2 Å.   In the curve fitting analyses, the backscattering amplitude and the phase shift were calculated by FEFF 6L using the following measures as fitting parameters: the number of neighboring atoms, interatomic distances between the absorbed atoms and the neighboring atom, Debye-Waller factor and absorption edge energy. The intrinsic loss factor was obtained from the curve fitting analysis of the EXAFS data of [Au(OH)$_4$]$^-$ solution which prepared by NaAuCl$_4$·2H$_2$O dissolved in NaOH solution.

TG/DTA measurement for the Au solid sample was performed by using TG/DTA7300 (HITACHI) between 298 K and 773 K with a heating rate of 0.5 K/min in air.   The weight of the Au solid sample was 37 mg and α-Al$_2$O$_3$ powder was used as reference material.

The ATR-IR spectrum of the Au solid sample was collected using Spectrum One FT-IR Spectrometer (Perkin Elmer, Inc.) at RT.   IR spectra were recorded from 4000-400 cm^{-1}.

Diffuse reflectance UV-Vis spectrum of the Au solid sample was measured using UV-3100PC Spectrophotometer (Shimadzu) at RT with BaSO$_4$ as a reflectance standard.   As light sources, a deuterium lamp and a tungsten lamp were used.   The spectrum was acquired from 200-800 nm.

O$_2$-TPR profile for the Au solid sample was obtained using BELCAT (BEL) equipped with a thermal conductivity detector (TCD).   The Au solid sample was calcined in a flow of 5 vol.% O$_2$/He (20 cm^3/min) at a heating rate of 0.5 K/min up to a final temperature of 773 K.   At the

same time, the analysis of gas generated by thermal decomposition reaction under 5 vol.% O_2/He flow was performed by using BEL-Mass (BEL).

In order to directly detect *in-situ* thermal decomposition reaction of the Au solid sample under hydrogen gas flow, *in-situ* XAS measurement in the temperature range from RT to 573 K with a heating rate of 5 K/min up to a final temperature 573 K was performed at BLl4B2 beamline of SPring-8.

H_2-TPR profile for the Au solid sample was obtained using BELCAT. The sample was heated in a flow of 5 vol.% H_2/Ar (20 cm^3/min) at a heating rate of 0.5 K/min up to a final temperature of 773 K. At the same time, the analysis of gas generated by thermal decomposition reaction under 5 vol.% H_2/Ar flow was performed by using BEL-Mass.

III-2-4   Determination of solubility of gold (III) hydroxide

By the above characterizations, the Au solid sample was determined to be gold (III) hydroxide ($Au(OH)_3$). Finally, the solubility of the gold (III) hydroxide at 298 K was measured. The equilibrium was approached from the both sides of supersaturation (the precipitation of $Au(OH)_3$) and of undersaturation (the dissolution of $Au(OH)_3$). In case of the superrsaturation system, the gold (III) hydroxide (13 mg) was added into water (100 cm^3) in a light shielding bottle to avoid the effects of light such as reduction to elemental gold. This solution was heated at 323 K for 4 days to attain the supersaturated condition under stirring magnetically. After cooling, pH and temperature were continuously monitored using a glass electrode equipped with a pH meter. At adequate intervals, aliquots of the suspension were taken out and filtrated with a 0.20 μm membrane filter for collection of filtrate. On the other hand, in case of the undersaturation system, the gold (III) hydroxide (65 mg) was added into water (500 cm^3) placed in a dark room to avoid the effects of light. The suspended solution was magnetically stirred. As well as the supersaturated system, pH and temperature were continuously monitored. At adequate intervals, aliquots of the suspension were taken out and

filtrated with a 0.20 μm membrane filter for collection of filtrate.   The concentration of gold in these filtrates was determined by AAS (AA-6300, Shimadzu).

III-3   Results and discussion

When HAuCl$_4$ solution was added into Na$_2$CO$_3$ solution, the precipitate was formed. Here, the precipitate is called "Au solid sample" as described in the experimental section.

III-3-1   Characterization of the Au solid sample

III-3-1-1   XRD

The XRD patterns of the Au solid sample and the standards are displayed in Fig. III-1. The XRD pattern of the Au solid sample (a) showed broad diffraction peaks at $2\theta = 32.5$ ° and 60.0 °.   No diffraction peak assigned to crystalline Au$_2$O$_3$ (b) and bulk Au (0) (c) appeared. The Au solid sample was X-ray amorphous.

III-3-1-2   TEM

Figure III-2 shows the TEM image (a) and the electron diffraction pattern (b) for the Au solid sample.   From the TEM image (a), the particle size of the Au solid sample was 8.83±3.47 nm and its shape was spherical.   Furthermore, the lattice image was slightly observed.   In order to examine whether the Au solid sample was crystalline, the electron diffraction pattern (b) was measured.   Although the XRD pattern showed that the Au solid sample was amorphous, the electron diffraction pattern suggests that the Au solid sample was slightly crystalline, because the diffraction ring and spots appeared as shown in Fig. III-2 (b).   The formation of crystalline Au$_2$O$_3$ by dehydration under high-vacuum is known empirically. Thus, the observed lattice image may be considered due to this empirical fact.

III-3-1-3 ^{197}*Au Mössbauer spectroscopy*

In order to examine the valence state of Au of the Au solid sample, ^{197}Au Mössbauer spectra were measured. Figure III-3 shows the ^{197}Au Mössbauer spectra for the Au solid sample (a) and Au foil (b) as a standard of Au (0). The spectrum for the Au solid sample showed only a peak with positive isomer shift. The ^{197}Au Mössbauer parameters are tabulated in Table III-1. In ^{197}Au Mössbauer spectroscopy, the different chemical state of Au can be separately detected depending on the isomer shift (IS) and the quadrupole splitting (QS). Figure III-4 shows the relationship between IS and QS for ^{197}Au Mössbauer parameter [29]. The two shadow parts in Fig. III-4 indicate the regions of the valence states which correspond to linearly coordinated Au (I) compounds and planar coordinated Au (III) compounds. The values of IS and QS were 2.66 and 1.87, suggesting that Au in the Au solid sample can be assigned to Au (III).
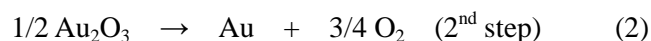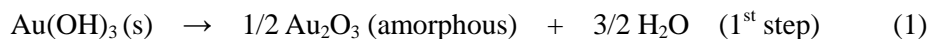
III-3-1-4   XAS

In order to identify atoms coordinated to Au (III) in the Au solid sample and to analyze the structure, XAS for the Au solid sample and the standard materials were measured. Figure III-5 shows the Au L_3-edge XANES spectra for $KAuCl_4$ (a) as a standard of Au (III) coordinating Cl^-, $[Au(OH)_4]^-$ solution (b) as a standard of Au (III) coordinating OH^-, the Au solid sample (c) and Au foil (d) as a standard of Au (0). The Au L_3-edge XANES spectrum for the Au solid sample showed a white line at 11.92 keV which indicates ionic character. The XANES spectrum for the Au solid sample was different from that for $KAuCl_4$. The peak at approximately 11.935 keV of $KAuCl_4$ is considered to be due to Au-Cl interaction[30]. However, no peak appeared at approximately 11.935 keV in the spectrum of the Au solid sample, suggesting that no Au-Cl interaction is present. Although gold has stable oxidation states of Au (I) and Au (III), Au_2O and AuCl, which are Au (I) compounds, are unstable with the exception of gold (I) cyanide. In

addition, the XANES spectrum for the Au solid sample was resembled with that for $[Au(OH)_4]^-$ solution.   From the facts, the oxidation state of Au in the Au solid sample is demonstrated to be Au (III), as supported from the result of ^{197}Au Mössbauer measurement.   Figure III-6 shows the Fourier transform of EXAFS oscillation Au L_3-edge spectra for KAuCl$_4$ (a), $[Au(OH)_4]^-$ solution (b), the Au solid sample (c) and Au foil (d).   In Fig. III-6, the peak at 1.8 Å, 1.6 Å and 2.5 Å can be assigned to Au-Cl interaction (a), Au-O interaction (b) and Au-Au interaction (d), respectively.   Thus, the peak at 1.6 Å of the Au solid sample can be assigned to Au-O interaction.   The EXAFS fitting parameters are shown in Table III-2.   The theoretical radial structure functions fit well with the experimental one, as evidenced by a R-factor of 0.372 %. The Debye-Waller factor (σ^2) and the energy origin shift (ΔE_0) obtained from $[Au(OH)_4]^-$ were used for the fitting analysis.   From the fitting model, the coordination numbers of Au-O was calculated to be 3.63±0.37.   From the curve fitting analysis of the EXAFS of the Au solid sample, the coordination number of Au (III) in the Au solid sample was considered to be four that is the same as $[Au(OH)_4]^-$.   As the Debye-Waller factor (σ^2), that a measure of the distribution of Au-O bond, is small, the Au solid sample can be considered to consist of a single phase.

III-3-1-5   TG/DTA

The Au solid sample was formed when HAuCl$_4$ solution was added into Na$_2$CO$_3$ solution and the Au-Cl interaction was not included in the Au solid sample as described above. Therefore, the Au solid sample could be considered to be gold (III) hydroxide (Au(OH)$_3$) or hydrous gold (III) oxide (Au$_2$O$_3$·nH$_2$O).   To accurately determine the chemical composition, the thermogravimetry (TG) for the dehydration reaction is useful.   The TG/DTA curves for the Au solid sample at 303-773 K are presented in Fig. III-7.   From the TG curve, the weight of the Au solid sample was decreased independently by 2 steps and the total weight loss was 18% until 773 K.   For the DTA curve, two sharp endothermic peaks were observed around 310 K

and 570 K.　As the experimental result, the weight loss for first and second steps were 8.4 %

and 9.6 %, respectively.　If the Au solid sample is gold (III) hydroxide ($Au(OH)_3$), the first step

reaction is due to dehydration from $Au(OH)_3$ and the formation of Au_2O_3 and the seconds step

reaction is due to the thermal decomposition of Au_2O_3 to Au.　These reactions are represented

as eqs.(1) and (2).

$$Au(OH)_3 (s) \quad \rightarrow \quad 1/2 \ Au_2O_3 \ (amorphous) \quad + \quad 3/2 \ H_2O \quad (1^{st} \ step) \qquad (1)$$

$$1/2 \ Au_2O_3 \quad \rightarrow \quad Au \quad + \quad 3/4 \ O_2 \quad (2^{nd} \ step) \qquad (2)$$

The endothermic peaks on the DTA curve can be assigned to the two reactions of eqs. (1) and

(2).　The theoretical thermal weight loss is 10.9 % for the first step reaction and 9.7 % for the

second step reaction, respectively.　Consequently, the experimental values for TG almost

coincided to the theoretical values as represented in Table III-3, suggesting that the Au solid

sample is gold (III) hydroxide ($Au(OH)_3$).　If the Au solid sample is hydrous gold (III) oxide

($Au_2O_3 \cdot nH_2O$), the experimental values of thermal weight loss may be more different from the

theoretical values and the first endothermic peak may not appear on the DTA curve because of

various temperature of dehydration.

　　　　Consequently, the coordination number of Au (III) in the Au solid sample and the

composition were considered to be four and $Au(OH)_3$, respectively, from Tables III-2 and III-3.

Based on the results, the structure of $Au(OH)_3$ can be proposed as shown in Fig. III-8.

　III-3-2　Chemical and physical properties of Au(OH)₃

　　III-3-2-1　IR spectrum

　　　　ATR-IR spectra for $Au(OCOCH_3)_3$ (a) as standard of the Au-O interaction, wet $Au(OH)_3$

(b) and dry $Au(OH)_3$ (c) are shown in Fig. III-9.　The absorptions of the wet $Au(OH)_3$ (b)

around 3500 cm^{-1} and 1600 cm^{-1} were large compared with those of the dry $Au(OH)_3$ (c).　This

is due to the increase in the absorption assigned to H-O-H and O-H group.　On the other hand,

all samples showed the broad absorption in the region of 900-400 cm^{-1}, especially there was the

strong absorption at 575 cm^{-1}.   Miyako and Susannah reported that the absorptions at 442 cm^{-1} and 426 cm^{-1} can be assigned to the Au-O stretching mode for cis-$(CH_3)_2Au(O,O'$-acac$)$ [31]. Thus, the absorption around 500 cm^{-1} may be assigned to the Au-O stretching mode for Au(OH)$_3$.

III-3-2-2   UV-Vis spectrum

The color of Au(OH)$_3$ prepared in this investigation was brown.   The UV-Vis spectrum associated with Au(OH)$_3$ is displayed in Fig. III-10.   Both the peak associated to $[AuCl_4]^-$, which is a starting material of Au(OH)$_3$, around 314 nm [11] and the peak for the surface plasmon resonance of Au nanoparticles around 520 nm [32] did not appear.   On the other hand, it showed the broad reflectance spectrum around 720 nm.

III-3-2-3   O$_2$-TPR profile

Gold nanoparticle supported metal oxide, which are representative supported gold catalysts, are often prepared by calcination of metal hydroxide sorbing Au(OH)$_3$ under air.   Therefore, thermal decomposition of Au(OH)$_3$ was examined in the presence of oxygen by the measurement of O$_2$-TPR profile.   In addition, the gas generated during the calcination was detected at the same time using the quadrupole mass spectrometer.   The obtained O$_2$-TPR profile and the quadrupole mass spectra for O$_2$ (a) and H$_2$O (b) are shown Figs. III-11 and III-12, respectively.   Figure III-13 shows a schematic diagram of TPR device.   The generated gas was directly introduced in the mass spectrometer.   On the other hand, water vapor was removed before gas was introduced in the TPR device.   On the mass spectra, the release of O$_2$ and H$_2$O was revealed in principle.   On the other hand, on the TPR profile, only release of O$_2$ was detected.   In the quadrupole mass spectra (Fig. III-12), H$_2$O (b) was detected from the initial step of the reaction, suggesting that the desorption of the adsorbed water, and then the elimination of H$_2$O molecule from Au(OH)$_3$ by condensation of OH groups were occurred

during the initial step of the reaction.　The generation of O_2 was detected on the TCD signal (Fig. III-11) and the mass spectrum (Fig. III-12 (a)) at 540 K, respectively.　It is due to the second reaction of the thermal decomposition reaction of Au_2O_3 as described above.　The results in Figs. III-11 and III-12 coincided to those from the result of TG/DTA as shown in Fig. III-7.

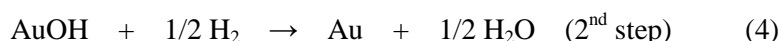### III-3-2-4　*Reduction process of Au(OH)₃ under hydrogen gas flow*

III-3-2-4-1　*In-situ XAS for Au(OH)₃ under hydrogen gas flow*

The supported gold catalysts are sometime prepared by calcination of metal (M) hydroxide sorbing $Au(OH)_3$ under hydrogen gas flow[33].　In the calcination reaction, an alloy (Au-M) was often formed.　The alloys are often useful catalysts for organic reactions [34].　Therefore, it is important to investigate the formation reaction of alloy, especially *in-situ*.　In this investigation, the reduction of $Au(OH)_3$ to Au (0) (elemental gold) was examined as a basic reaction for the formation of alloy.　Figure III-14 (b) shows the *in-situ* Au L_3-edge XANES spectra for $Au(OH)_3$ under hydrogen gas flow at RT-573 K.　The XANES spectra for $Au(OH)_3$ (a) as a standard of Au (III),and Au foil (c) as a standard of Au (0) are also shown in Fig. III-14 together.　In Fig. III-14 (b), the intensity of white line at 11.92 keV decreased with increasing temperature under hydrogen gas flow.　The variation of ratio of Au (0) and Au (III), which is calculated from the intensity of white line at 11.92 keV under hydrogen gas flow, with temperature is shown in Fig. III-15.　The reduction of $Au(OH)_3$ was started at 373 K and was almost reduced at 473 K.　Fourier transform of *in-situ* EXAFS oscillation Au L_3-edge spectra for $Au(OH)_3$ (a), $Au(OH)_3$ under hydrogen gas flow at RT-573 K (b) and Au foil (c) are shown in Fig. III-16.　In Fig. III-16, the peak at 1.6 Å and 2.5 Å can be assigned to Au-O interaction (a) and Au-Au interaction (c), respectively.　For the calcination of $Au(OH)_3$, the peak due to Au-O interaction was observed below 423 K, on the other hand, the peak due to Au-Au interaction appeared above 373 K.　Suggesting that the thermal decomposition reaction under

hydrogen gas flow of Au(OH)$_3$ is started with an increase in temperature, and then Au(OH)$_3$ is almost reduced to Au (0) (elemental gold) at 473 K.

III-3-2-4-2   H$_2$-TPR profile

In order to obtain information on the more detailed thermal decomposition reaction of Au(OH)$_3$ accompanying the reduction to Au (0) (elemental gold) under hydrogen gas flow at RT-773 K, H$_2$-TPR profile was observed.   In addition, the quadrupole mass spectra were measured at the same time to detect the release of H$_2$O and the consumption of H$_2$ during the calcination reaction.   The results of H$_2$-TPR profile and the quadrupole mass spectra for H$_2$ (a) and H$_2$O (b) are shown Figs. III-17 and III-18, respectively.   In Fig. III-17, the four TCD signals were observed between 335 K and 535 K.   On the other hand, in the quadrupole mass spectra (Fig. III-18), the peak assigned to the hydrogen consumption between 360 K and 373 K (a), and the two peaks assigned to the release of H$_2$O at 360 K and 373 K were observed (b). These reactions may be associated with the reduction of the Au(OH)$_3$ to Au (0) (elemental gold) because of the Au (III) in the Au(OH)$_3$ was almost reduced to Au (0) (elemental gold) until 473 K based on the result of the *in-situ* Au L$_3$-edge XAS spectra in Figs. III-14~III-16.   Moreover, in Fig. III-18 (b), H$_2$O was released two times at 360 and 373 K, suggesting the separate reduction reaction, that is, Au (III) to Au (I) and Au (I) to Au (0).   In a chemistry of gold, it is well known that stable compounds of Au(I) and Au(III) are present.   Thus, these reaction assigned to the thermal decomposition reaction of Au(OH)$_3$ under hydrogen gas flow can be concluded to be the different 2 steps reactions as eqs. (3) and (4).

$$Au(OH)_3 (s)   +   H_2   \rightarrow   AuOH   +   2\,H_2O   (1^{st}\,step)   \quad (3)$$

$$AuOH   +   1/2\,H_2   \rightarrow   Au   +   1/2\,H_2O   (2^{nd}\,step)   \quad (4)$$

In the eqs. (3) and (4), the consumption of H$_2$ should be occurred two times around 360 and 373 K.   In Fig. III-17, the peaks (i) and (ii) were considered to be the consumption of H$_2$ in the eqs. (3) and (4).   Although the peak (iii) cannot be assigned, the peak (iv) observed between 470 K and 540 K may be due to the change in the thermal conductivity by dissociative adsorption of

H_2 molecule on the Au nanoparticles[35] from the correspondence of the peak indicated by *
assigned to H_2 consumption in Fig. III-18 (a).

III-3-2-5　Solubility of Au(OH)$_3$

The solubility of metal hydroxide (g / 100 g of H_2O) is one of the most basic properties in
chemistry.　The solubility equilibrium of metal hydroxide is generally attained by two ways:
(1) dissolution of metal hydroxide in water and (2) precipitation of metal hydroxide from a
supersaturated solution.　Here, the solubility of Au(OH)$_3$ was measured through the two ways.
First, an excess of Au(OH)$_3$ was added into water and the variation of Au concentration in water
with time was measured in air conditioned room to maintain a constant temperature.　At the
same time pH and temperature of the water were also monitored.　Second, a supersaturated
solution with respect to Au(OH)$_3$ at 298 K was prepared by dissolving Au(OH)$_3$ in hot water.
After cooling to RT, the same measurements were carried out.　Figure III-19 shows the
variations of Au concentration in water with time.　The result includes those from the
undersaturation condition (1) and from the supersaturation condition (2).　In case of (1) the Au
concentration increased with time.　On the other hand, in case of (2) the Au concentration
decreased with time.　Finally, these Au concentrations approached to a constant value (0.00124
g/100 g of H_2O in case of (1) and 0.00137 g/100 g of H_2O in case of (2)).　The each
experimental results are shown in Table III-4.　After 440 h, Au concentration in each
experiment was almost the same, suggesting that the solubility equilibrium was attained.　From
the two experiments, a mean Au concentration after 440 h was calculated to be 0.00131 g/100 g
of H_2O. This value can be considered to be the solubility of Au(OH)$_3$ at 297 K which was the
temperature during the experiment.　There is an old report about the solubility of Au(OH)$_3$ by
Herrick and Hollis[27].　They reported that the solubility of Au(OH)$_3$ in pure water was
obtained to be 0.00769 g/100 g of H_2O by using a potentiometric titration.　However, the
solubility of Au(OH)$_3$ in the previous paper was slightly higher than that in this investigation.
The difference may be due to different experimental method.

The pH value was almost constant during the two solubility measurements. The pH values are also given in Table III-4. No change in pH suggests that H^+ or OH^- ion does not participate to the dissolution reaction of $Au(OH)_3$. In addition, Au^{3+} ion has a square planar structure due to its electronic structure and its coordination number is four. Therefore, the dissolution reaction of $Au(OH)_3$ may be represented as eq. (5).
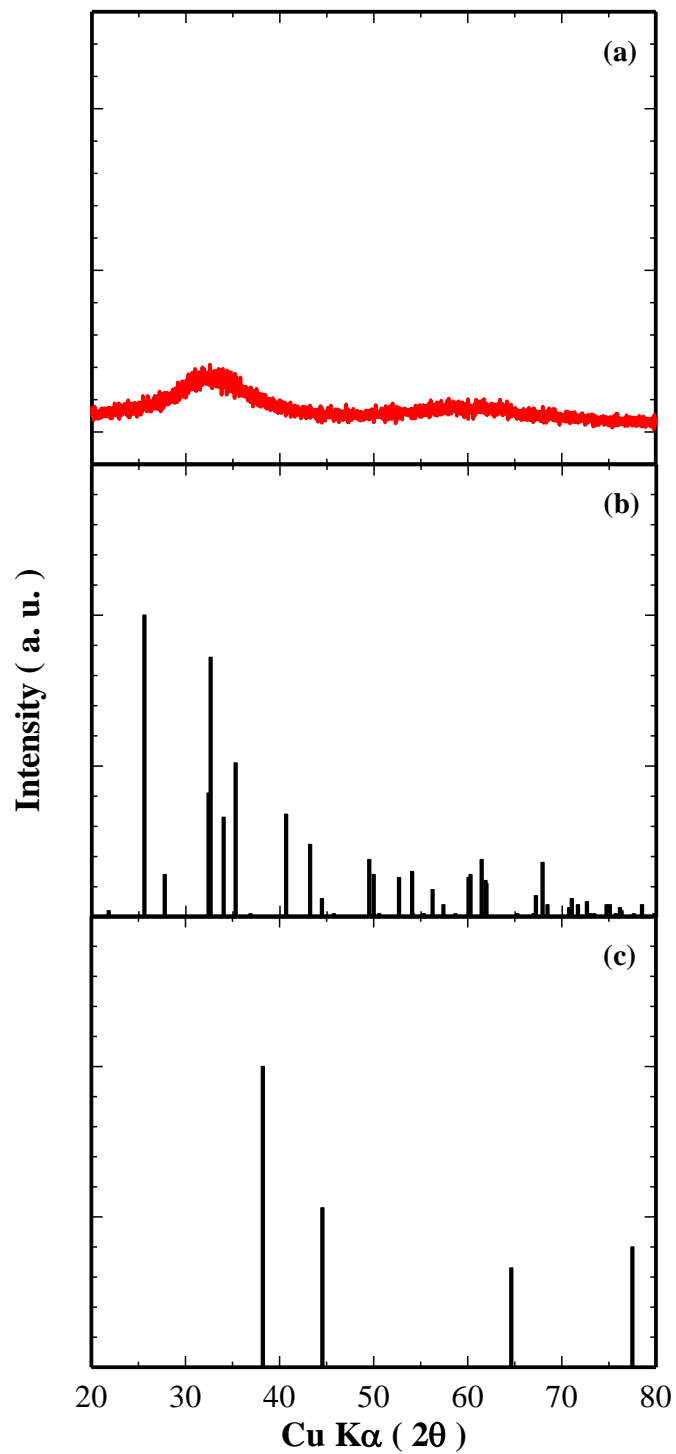
$$Au(OH)_3 \text{ (solid)} \quad + \quad H_2O \text{ (liquid)} \quad \rightarrow \quad [Au(OH)_3(H_2O)]^0 \text{ (aqueous species)} \qquad (5)$$

Fig. III-1　XRD patterns of the Au solid sample (a), Au_2O_3 (ICDD: 00-043-1039) (b)

and bulk Au (0) (ICDD: 00-001-1172) (c).

The diffractograms for Au_2O_3 and Au were given from data base (ICDD).
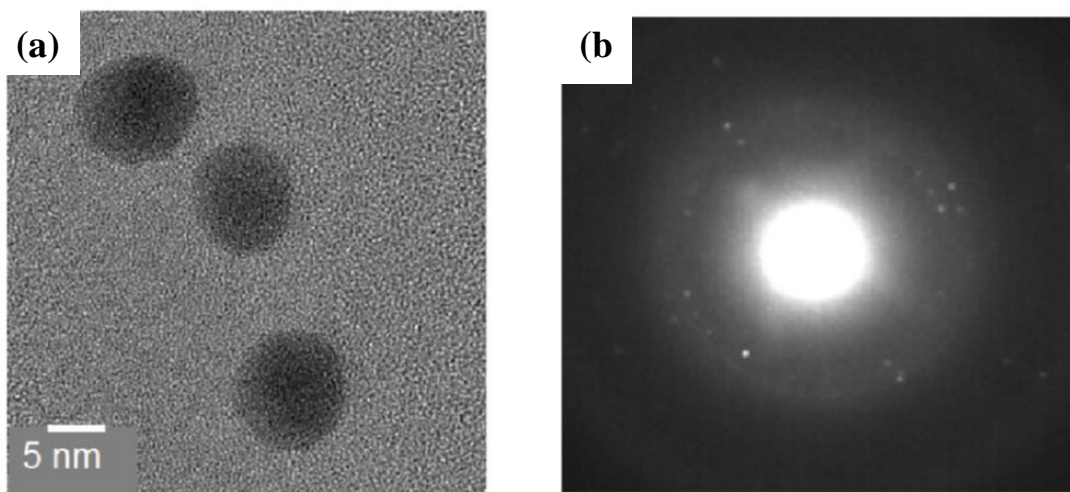
Fig. III-2   TEM image (a) and electron beam diffraction (b) for the Au solid sample.
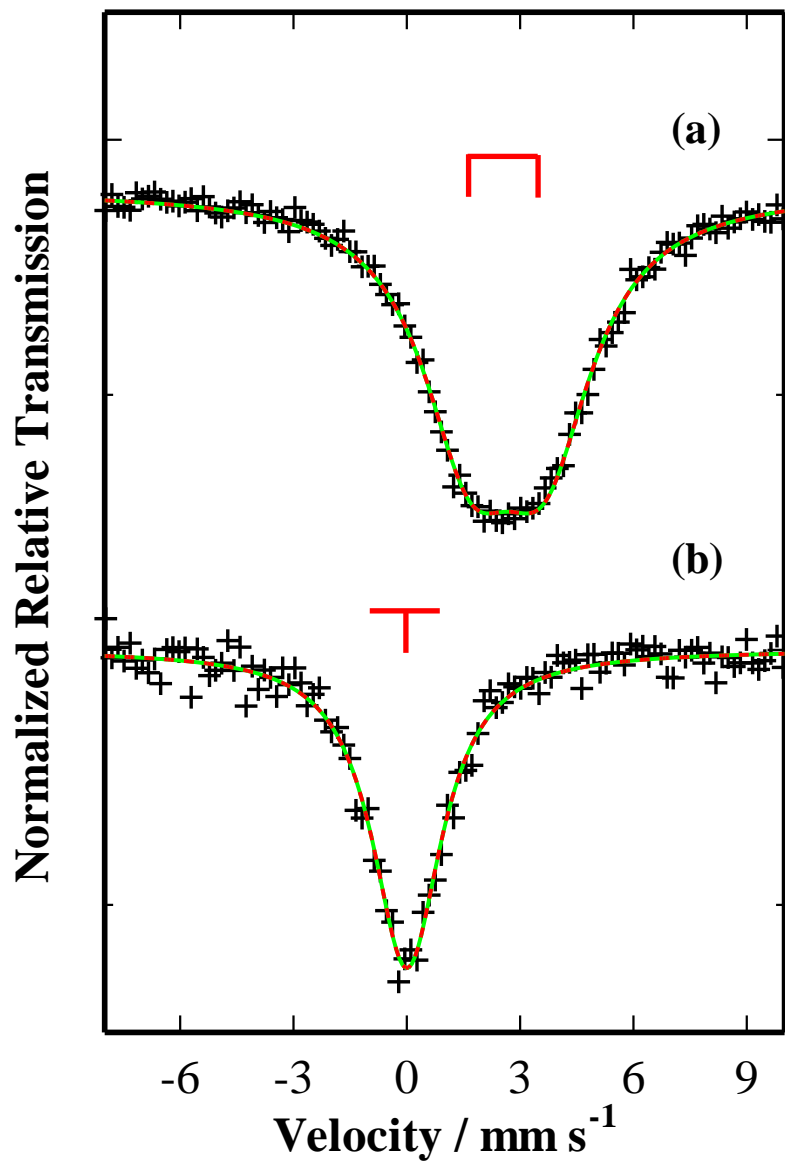
Fig. III-3   [197]Au Mössbauer spectra for the Au solid sample (a) and Au foil (b).

Table III-1 ^{197}Au Mössbauer parameters for Au foil and the Au solid sample.

Sample name	Mössbauer parameters	
	IS / mm s^{-1}	QS / mm s^{-1}
Au foil	0.00±0.02	-
Au solid sample	2.66±0.05	1.87±0.05
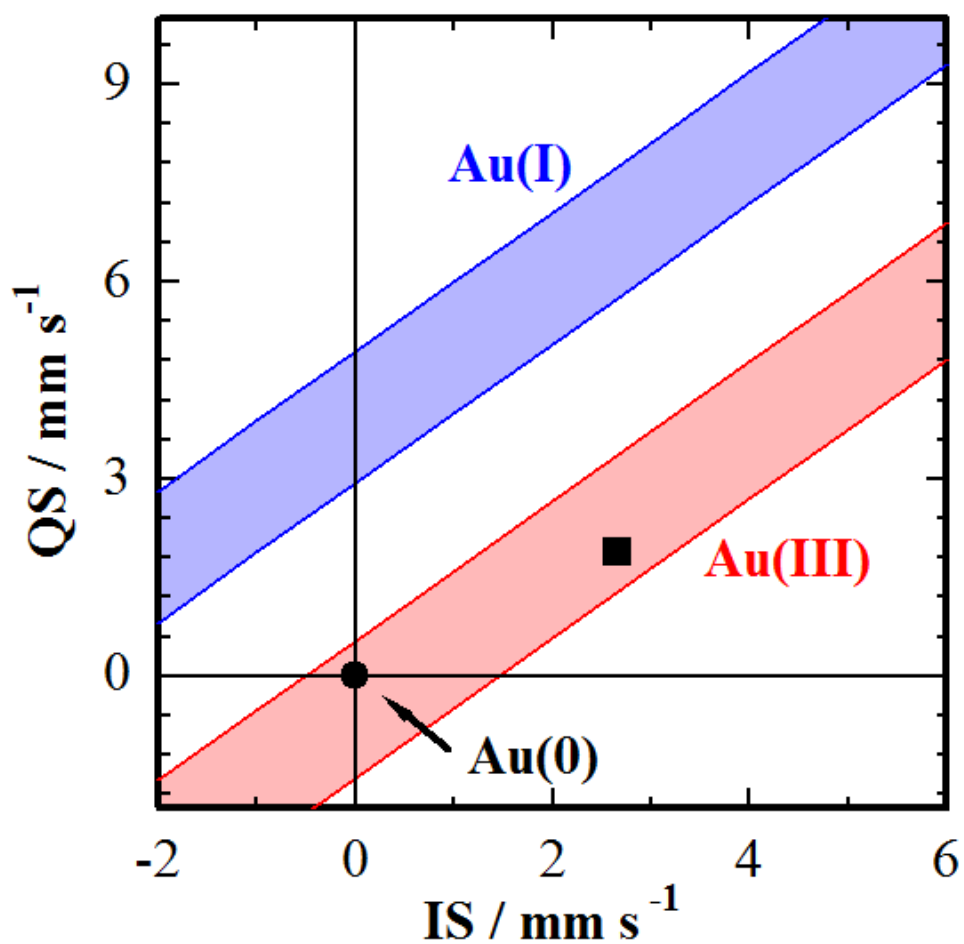
Fig. III-4 The relationship between IS and QS for [197]Au Mössbauer parameter[29].

The each region indicates the corresponding to linearly coordinated Au (I) compounds

and planar coordinated Au (III) compounds.

Their symbols are the Au solid sample (■) and Au foil (●), respectively.
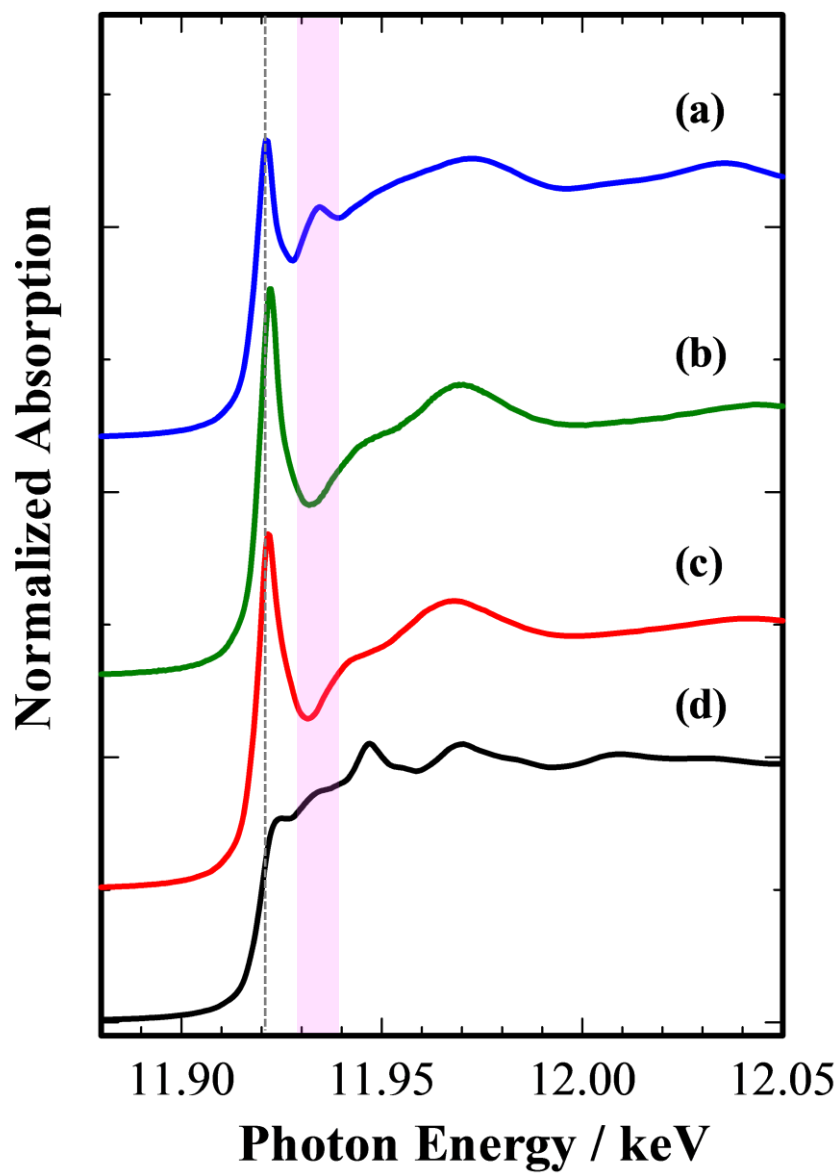
Fig. III-5   Normalized Au L_3-edge XANES spectra for $KAuCl_4$ (a), $[Au(OH)_4]^-$ solution (b),

the Au solid sample (c) and Au foil (d).
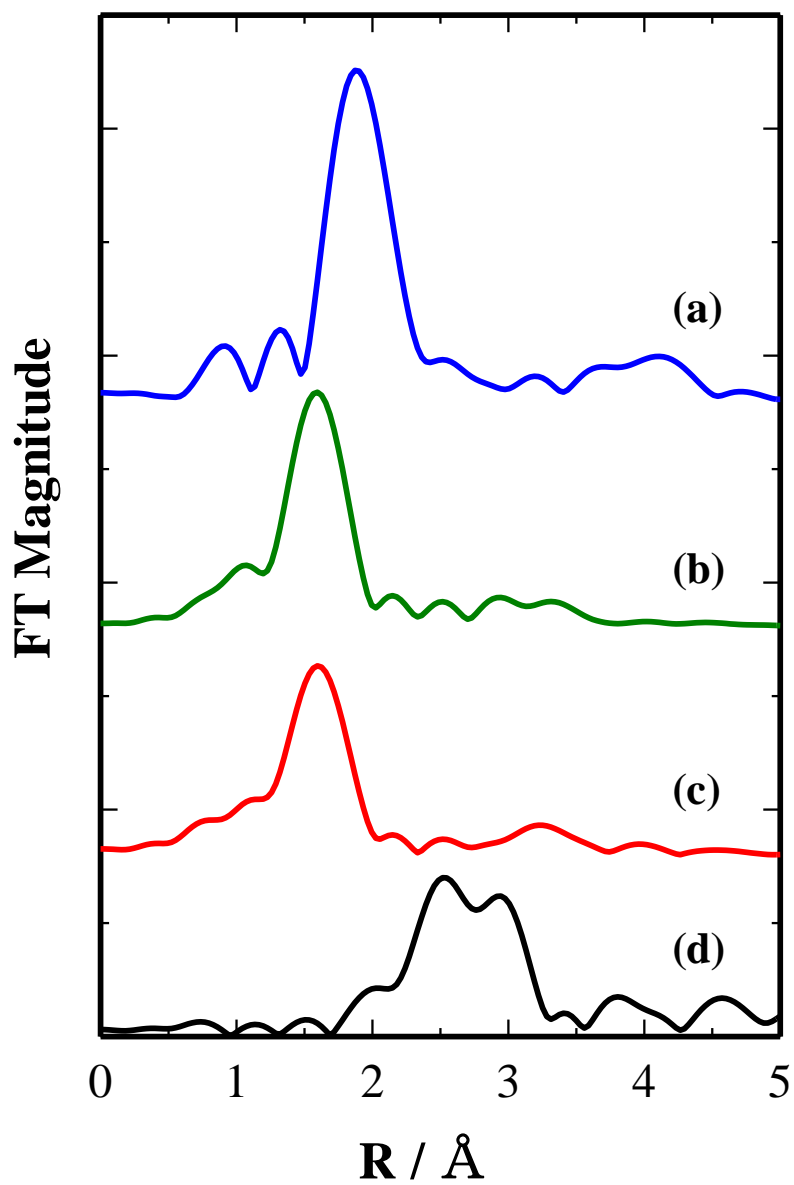
Fig. III-6   Fourier transform of EXAFS oscillation Au L_3-edge spectra for $KAuCl_4$ (a),

$[Au(OH)_4]^-$ solution (b), the Au solid sample (c) and Au foil (d).

Table III-2   EXAFS fit parameters for the Au solid sample

$(k^3: \Delta k = 3\text{-}12.5$ Å $^{-1}$ and $\Delta r = 1.0\text{-}2.0$ Å$)$.

Sample	Shells	CN[a]	R/ Å [b]	ΔE_0	σ^2/ Å $^{2[c]}$	R_{factor} (%)[d]
$[Au(OH)_4]^-$ solution	Au-O	4.0[e]	1.98±0.007	3.96±1.87	0.00227±0.0008	0.621
Au solid sample	Au-O	3.63±0.37	2.00±0.006	4.93±1.32	0.00353±0.0008	0.372

[a]: First shell coordination number.

[b]: Bond length.

[c]: Debye-Waller factor.

[d]: Goodness of fit index.

[e]: Coordination number was fixed as that of a square plane.
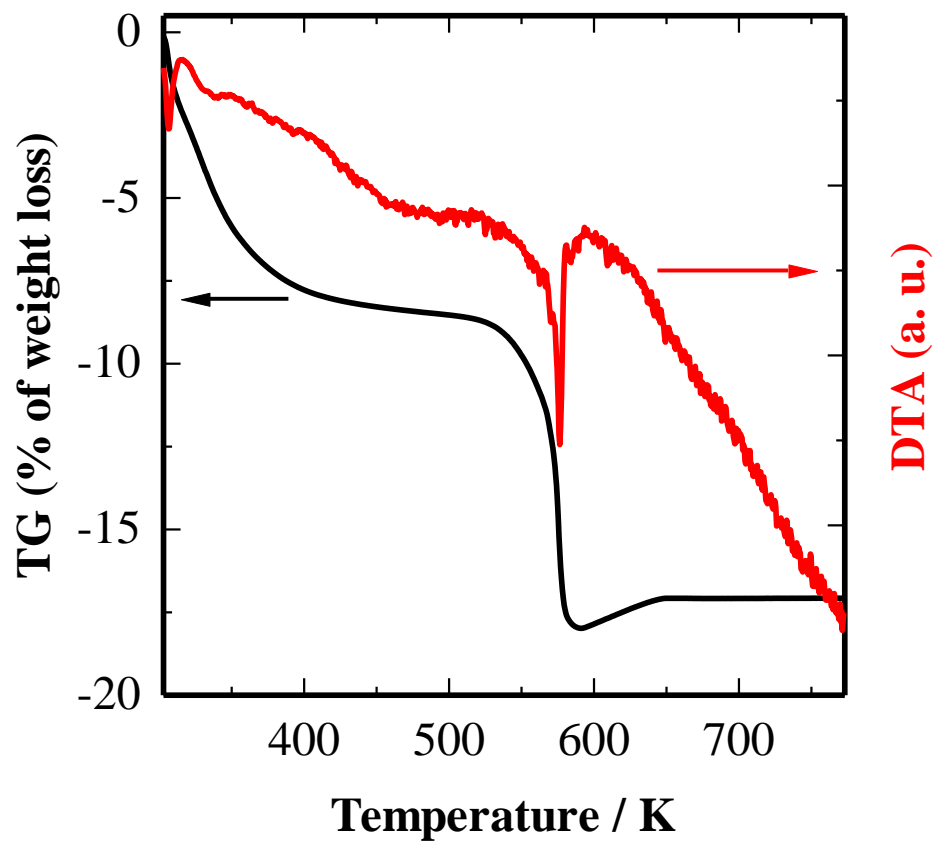
Fig. III-7　The TG/DTA curves for the Au solid sample.

Table III-3　The results for TG/DTA analyses.

Reaction	Calculated value (%)	Observed values (%)
1st step reaction	10.9	8.4
2nd step reaction	9.7	9.6
Total	20.6	18.0

The weight of the Au solid sample was 37.05 mg.
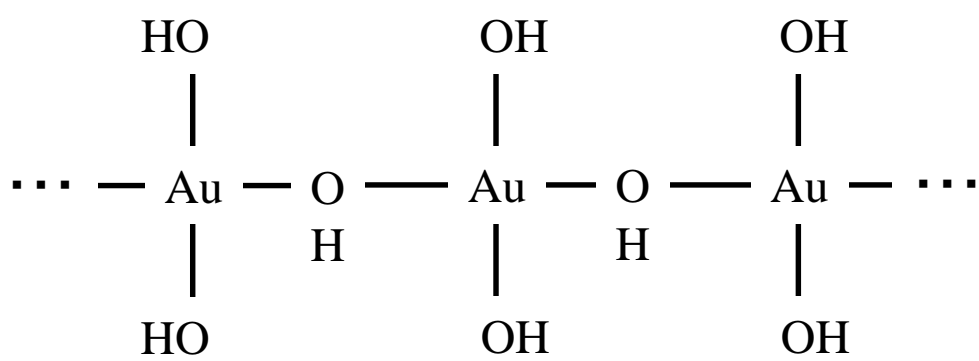
Fig. III-8   The structure of $Au(OH)_3$.
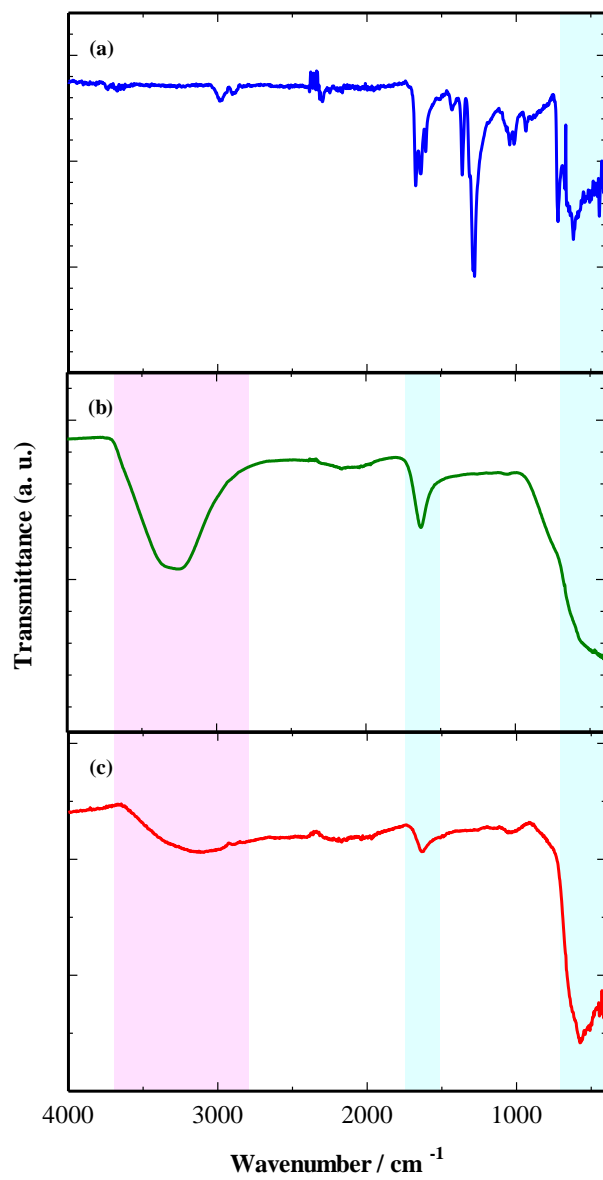
Fig. III-9　ATR-IR spectra for Au(OCOCH$_3$)$_3$ (a), wet Au(OH)$_3$ (b) and dry Au(OH)$_3$ (c).
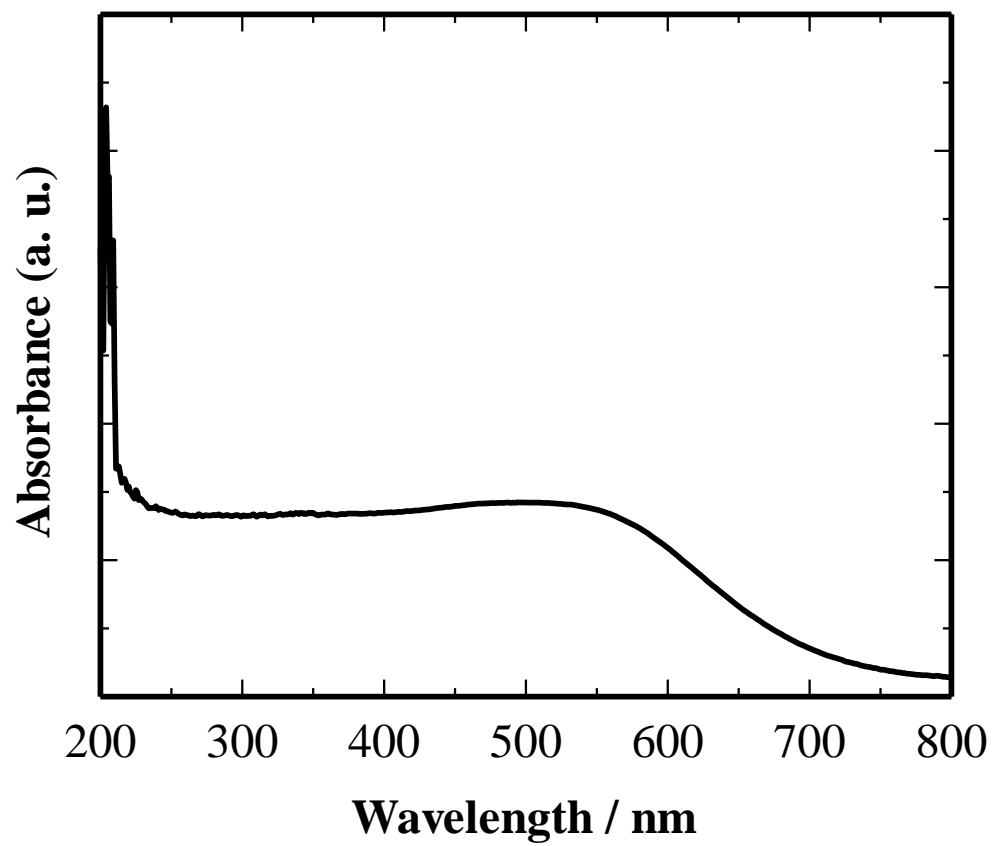
Fig. III-10　UV-Vis spectrum for solid Au(OH)$_3$.
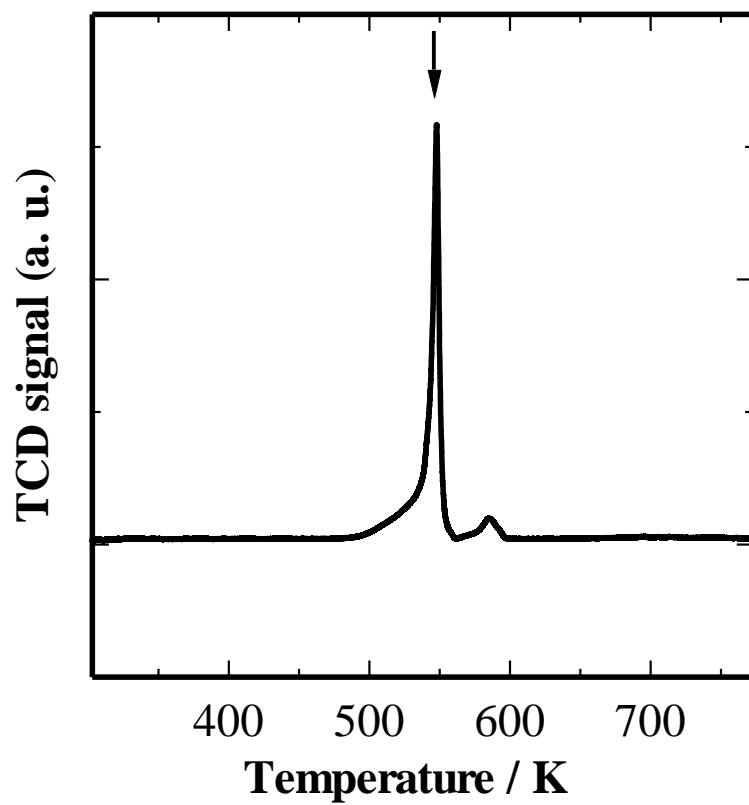
Fig. III-11   The O_2-TPR profile for Au(OH)$_3$.

Calcination temperature: RT-773 K.

Atmosphere: a flow of 5 vol.% O_2/He.
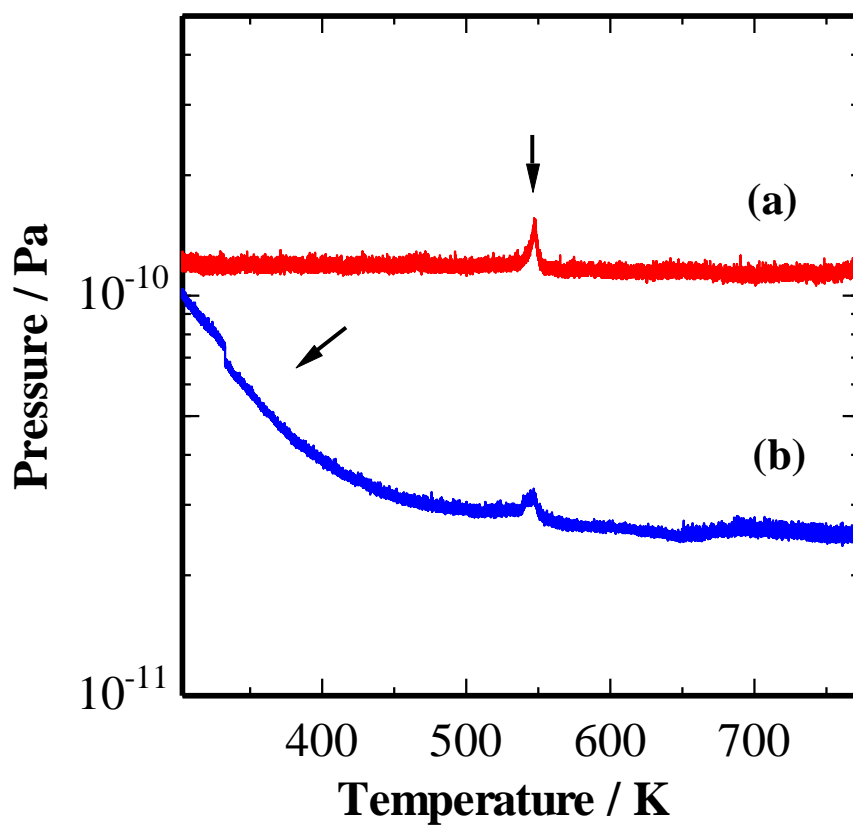
Fig. III-12   The quadrupole mass spectra

for O_2 (a) and H_2O (b) generated during calcination of $Au(OH)_3$.

Calcination temperature: RT-773 K.

Atmosphere: a flow of 5 vol.% O_2/He.
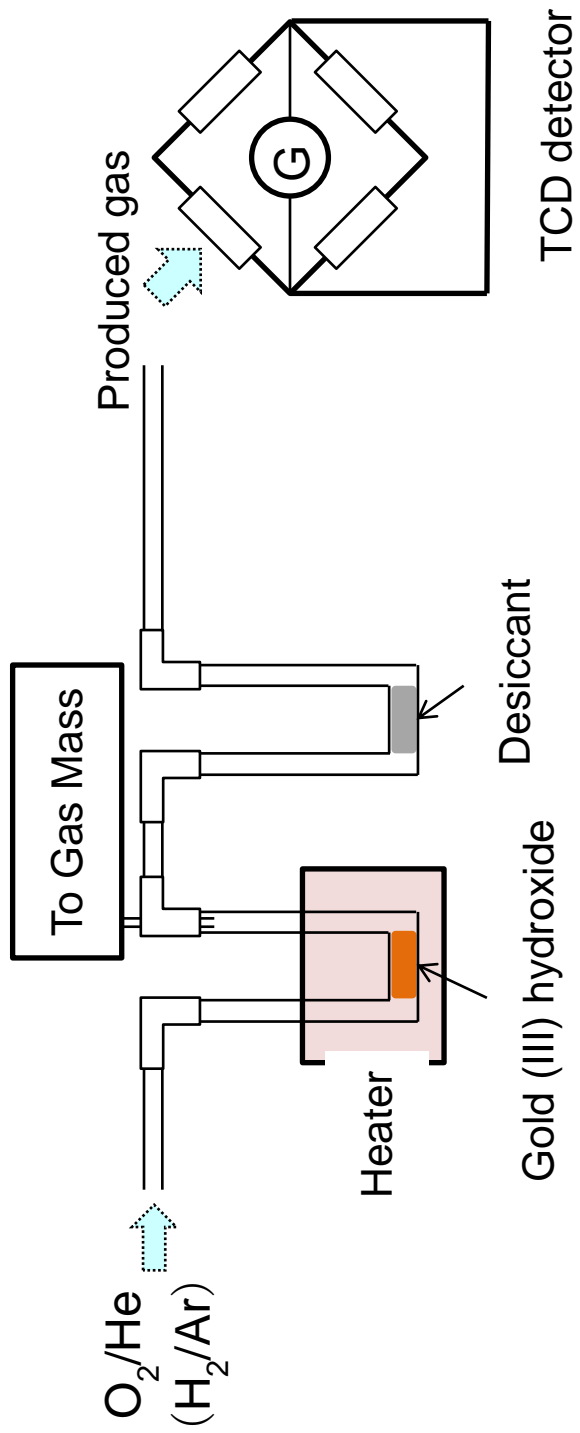
Fig. III-13 A schematic diagram of the TPR device.

O$_2$/He
(H$_2$/Ar)

To Gas Mass

Produced gas

TCD detector

Desiccant

Heater

Gold (III) hydroxide

G
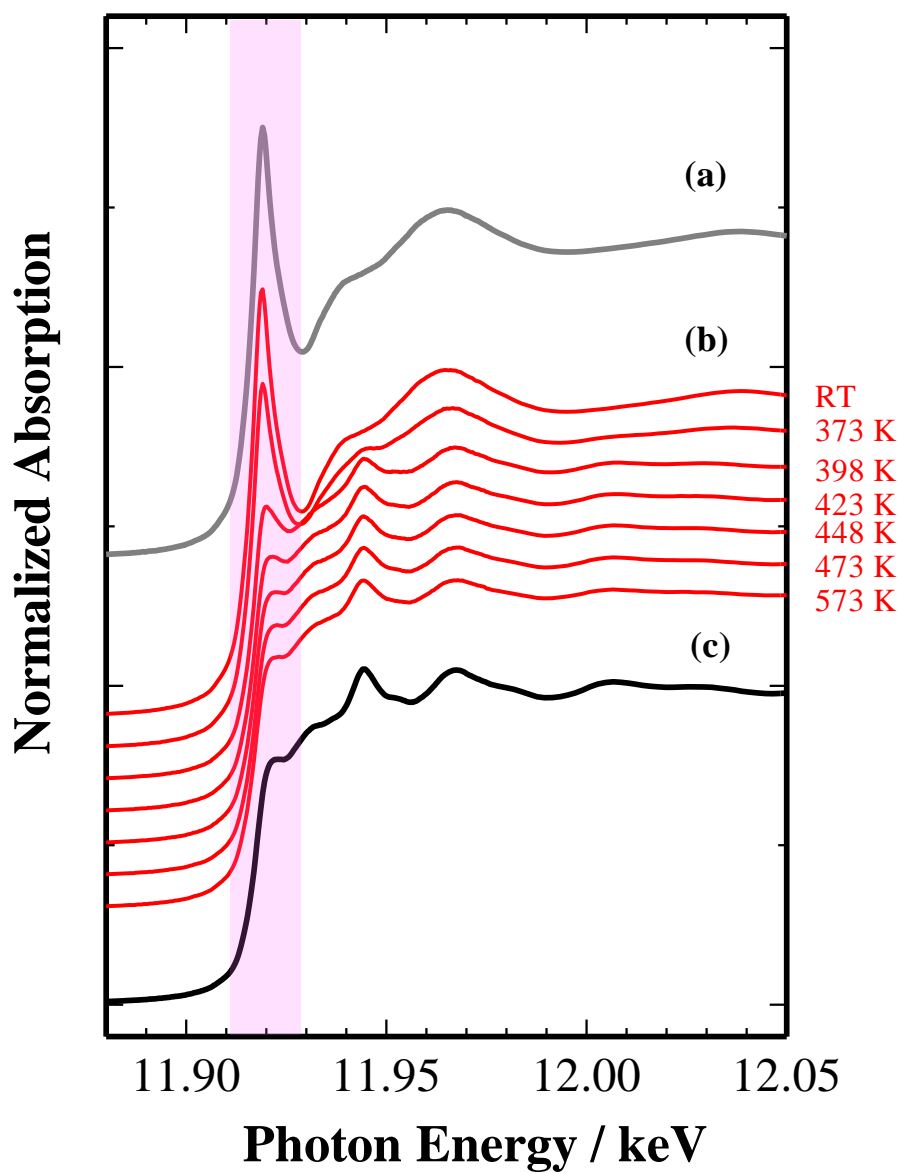
Fig. III-14   Normalized *in-situ* Au L$_3$-edge XANES spectra for Au(OH)$_3$ (a), Au(OH)$_3$

calcined (the numbers in the figure mean Kelvin absolute temperature) (b) and Au foil (c).

Spectra (a) and (c) were measured at RT.

Spectra (b) were measured at each temperature shown in the figure.

Calcination temperature: RT-573 K.

Atmosphere: under hydrogen gas flow.
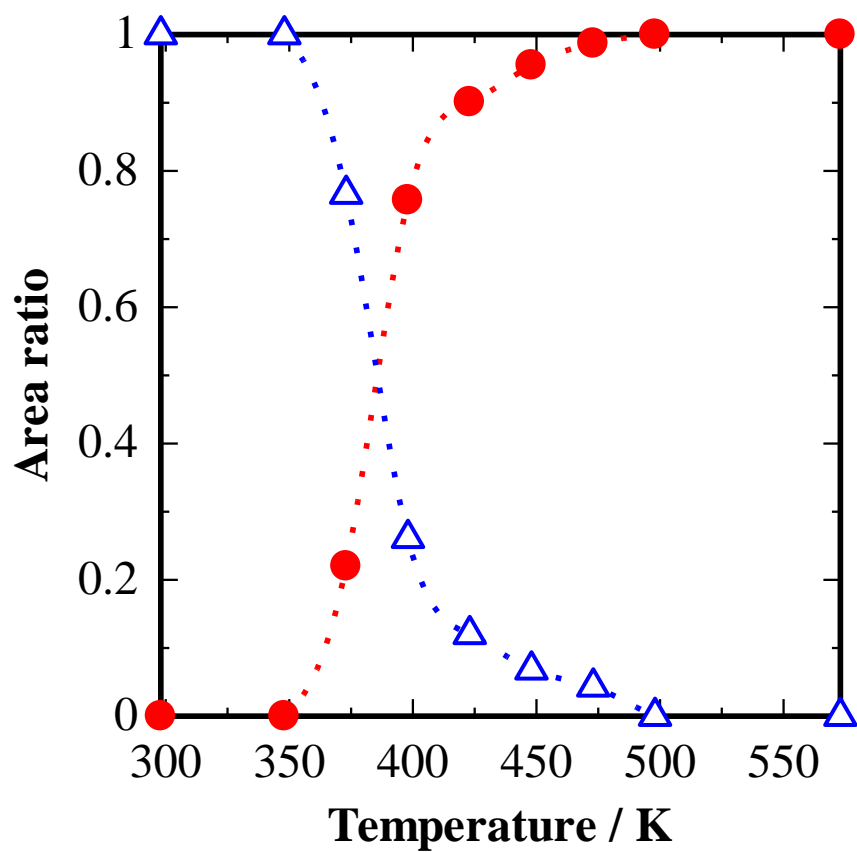
Fig. III-15   The variation of ratio of Au (0) (●) and
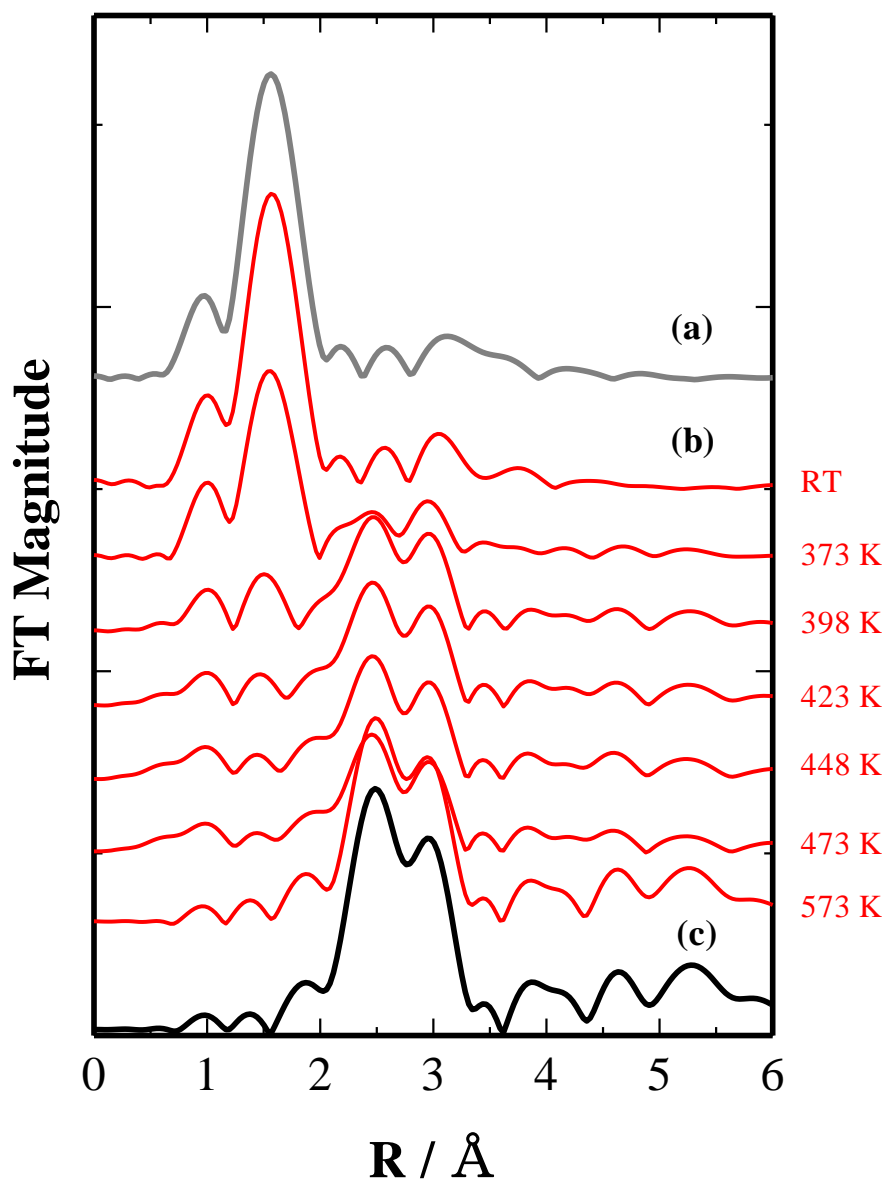the Au (III) (△) under hydrogen gas flow at RT-573 K.

Fig. III-16 Fourier transform of *in-situ* EXAFS oscillation Au L$_3$-edge spectra

for Au(OH)$_3$ (a), Au(OH)$_3$ calcined (b) and Au foil (c).

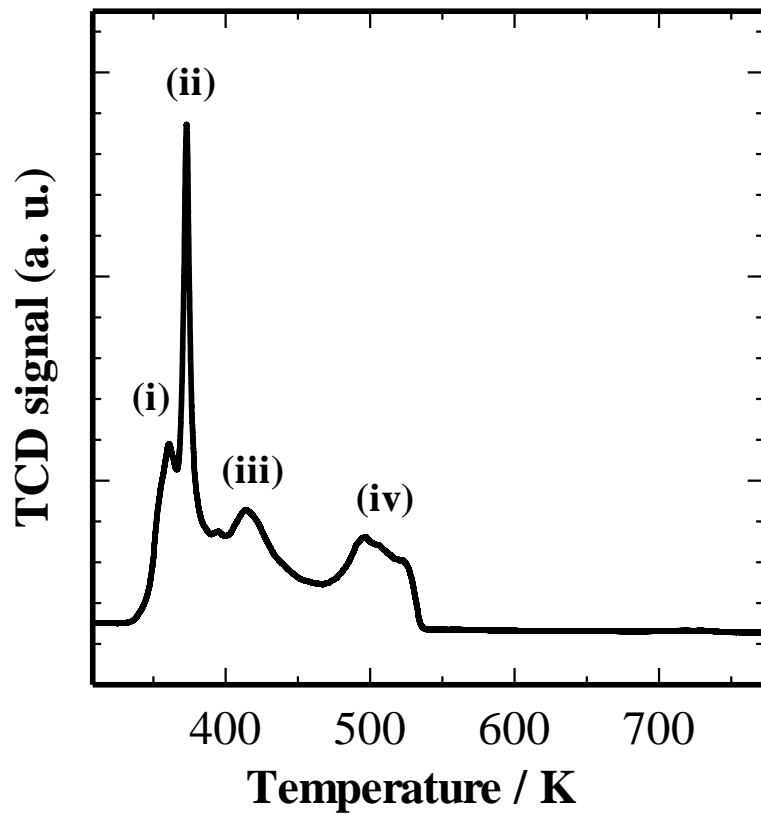Each peak in this figure corresponds to that in Fig. III-14.

Fig. III-17   The H_2-TPR profile for $Au(OH)_3$.

Calcination temperature: RT-773 K.
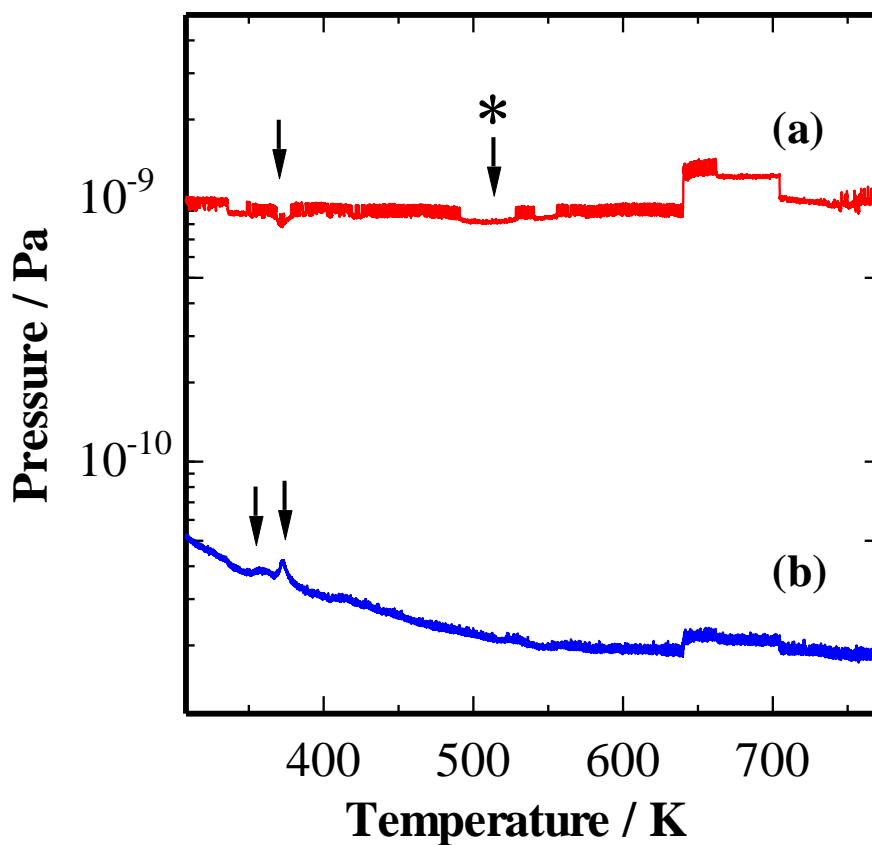
Atmosphere: a flow of 5 vol.% H_2/Ar.

Fig. III-18　The quadrupole mass spectra

for H_2 (a) and H_2O (b) during calcination of $Au(OH)_3$.

Calcination temperature: RT-773 K.

Atmosphere: a flow of 5 vol.% H_2/Ar.

The peak indicated by * was assigned to the consumption of H_2

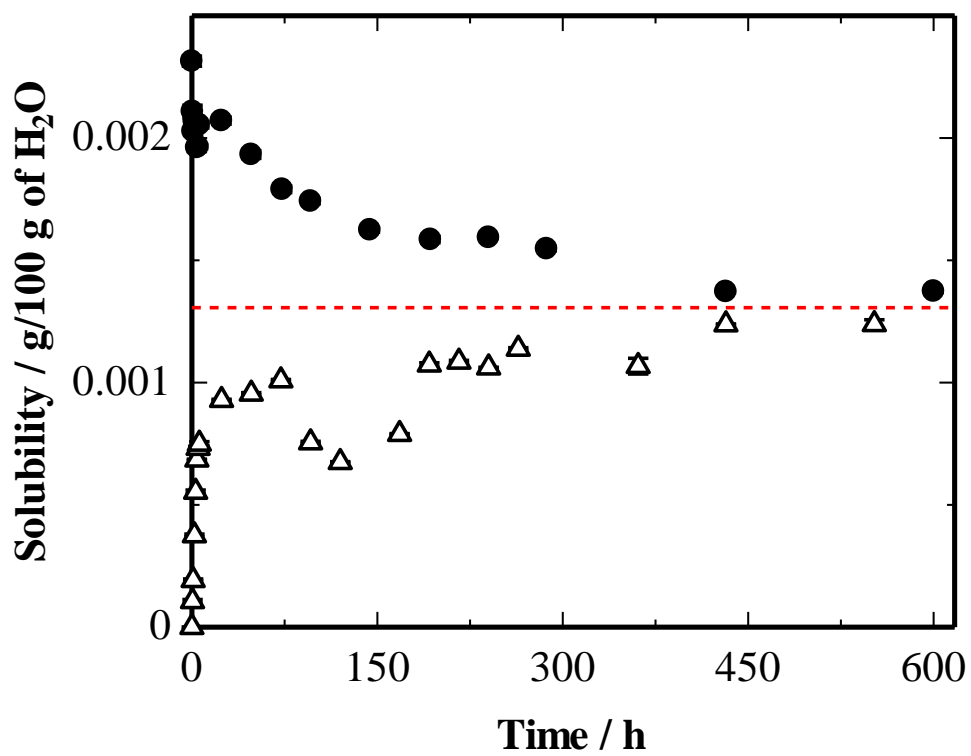by dissociative adsorption of H_2 molecule on the Au nanoparticles.

Fig. III-19　Solubility of Au(OH)$_3$ approached

both from the side of supersaturation and that of undersaturation.

Their symbols were the supersaturated system (●)

and the undersaturated system (△), respectively.

Table III-4　The result of the solubility measurements of $Au(OH)_3$

both of the supersaturated system and the undersaturated system.

System	Solubility / g/100 g of H_2O	pH	Temperature / K
Supersaturated system	0.00137±0.000006	6.05±0.31	296.9±0.81
Undersaturated system	0.00124±0.00002	6.06±0.27	297.5±0.75

Chapter IV

A novel preparation method of a single phase Au-Cu powder alloy and its characterization

IV-1   Introduction

In various fields, alloy has attracted attention because of their specific chemical and physical properties.   The noble metal alloys have also been studied extensively [25, 36].   In the metallurgical method which is a typical alloy preparation method, the alloy is formed by melting the component elements.   In this metallurgical method, there are three main problems: (1) a temperature above the melting point of the elemental metal component is necessary, (2) alloy with the desired composition is difficult to prepare if the optimum condition is impossible to attain, and (3) it is difficult to mold fine structures due to the different cooling conditions of liquid alloy with high temperature.   Recently, the preparation method of alloy using a chemical reaction has been studied because fine powder alloys can be obtained at lower temperatures than the metallurgical method.   Fine powder alloy consisting of a single phase is advantageous for building up fine structures by pressing.   As examples of the representative method to prepare powder alloys, the following methods are known: reduction of the precursor of alloy in solution [36, 37] and electrochemical method [38, 39].   In the former, a part of the component elements remain dissolved in the solution after the reaction.   On the other hand, in the latter, the mixture of metals of each component element is partly formed during the reaction.   Thus, it is difficult to control the uniform composition of the alloy in the conventional methods. Namely, the preparation of alloy consisting of a single phase is often impossible even by the use of these chemical reactions.

The supported gold catalyst is generally prepared by calcination of the precursor (coprecipitate of gold (III) hydroxide ($Au(OH)_3$) with metal hydroxide ($M(OH)_n$, ($n = 2$ or 3)) in

air at approximately 573 K [8, 40].   On the other hand, our research group found that when the precursor was calcined under hydrogen gas flow at 573 K, alloys composed of M and Au could be formed [33].   Based on this finding, I aimed to prepare powder alloys consisting of a single phase and the desired compositions at low temperature.   In this paper, I describe the preparation of an Au-Cu powder alloy that is used for catalyst [41, 42] and dental materials [43]. A characteristic of this preparation method is the use of a mechanical mixture of $Cu(OH)_2$ and $Au(OH)_3$ as a precursor to accurately control the composition (Au/Cu atomic ratio). Because in the coprecipitation of $Au(OH)_3$ with $M(OH)_n$ in solution, it is difficult to control precisely the composition (Au/M atomic ratio) of the precursor due to different mixing conditions of a mixed solution of Cu (II) and $[AuCl_4]^-$ and alkali solution such as Na_2CO_3 in every preparations. Moreover, in this study, I characterized the calcined *Sample* using X-ray absorption spectroscopy (XAS) for Cu and Au and ^{197}Au Mössbauer spectroscopy to elucidate the chemical state of Cu and Au in the Au-Cu powder alloy consisting of a single phase.

IV-2   Experimental

IV-2-1   Chemicals and Sample preparation

Reagents used in this study were of analytical reagent grade.   Solutions were prepared with deionized-distilled water. $Cu(NO_3)_2 \cdot 3H_2O$ and $HAuCl_4 \cdot 4H_2O$ were purchased from Wako Pure Chemical Industries, Ltd. and TANAKA HOLDINGS Co., Ltd., respectively.   An Au_5Cu_5 alloy as a standard of Au-Cu alloy was purchased from High Purity Materials KOJUNDO CHEMICAL LABORATORY Co., Ltd.. $Cu(NO_3)_2 \cdot 3H_2O$ (2.5 g) was dissolved into 50 cm^3 of water (343 K) and $[Cu(NH_3)_4]^{2+}$ was prepared by adding 10% NH_3 solution to the $Cu(NO_3)_2$ solution.   In order to prepare $Cu(OH)_2$, a stoichiometric 0.1 mol/dm^3 NaOH solution was added to the $[Cu(NH_3)_4]^{2+}$ solution.   The precipitate was filtered with 0.45 μm membrane filter, washed with water and then was air dried. Na_2CO_3 solution and $HAuCl_4$ solution were prepared by dissolving anhydrous Na_2CO_3 (4.9 g) into water (100 cm^3) and by dissolving $HAuCl_4 \cdot 4H_2O$ (4.0 g) into water (50 cm^3), respectively.   To prepare $Au(OH)_3$, the $HAuCl_4$ solution was mixed with the Na_2CO_3 solution, and the mixed solution was magnetically stirred for 8 h.   The obtained precipitate was filtered with 0.2 μm membrane filter, washed with water and then was freeze-dried under vacuum.   Subsequently, the Au-Cu powder alloy was prepared by calcination of the mixture of $Cu(OH)_2$ (163 mg) and $Au(OH)_3$ (413 mg) as a precursor (Au/Cu atomic ratio of 1) under hydrogen gas flow (flow rate: 20 cm^3/min) at 573 K for 4 h.

IV-2-2   Materials Characterization

XRD analysis of the samples was performed using Ultima IV (Rigaku) at a scanning rate of 2 °/min and at a step scan of 0.02 ° in the 2θ range of 20-80 ° with Cu Kα radiation.   The operating voltage and current were 40 kV and 30 mA, respectively.   The crystalline phase of the calcined *Sample* was identified according to the ICDD diffraction file.

For the XAS measurement, the calcined *Sample* was diluted with boron nitride (BN), and the pellet was made. The Cu K-edge and Au L_3-edge XAS were measured for the standard samples and the calcined *Sample* by transmission mode at BL14B2 beamline of SPring-8 (8 GeV and 99.5 mA). The XAS spectra of Au_5Cu_5 alloy were only measured by conversion electron yield mode at BL06 beamline of SAGA-LS(1.4 GeV). These measurements were conducted at RT. Moreover, in order to determine the formation process of the Au-Cu alloy from the precursor, *in-situ* XAS measurements of the mixture of $Cu(OH)_2$ and $Au(OH)_3$ under hydrogen gas flow were performed in the temperature range from RT to 573 K at BL14B2 beamline of SPring-8. The spectra were analyzed using software (Athena of Ifeffit) [15].

The [197]Au Mössbauer spectra were measured by transmission method at Research Reactor Institute of Kyoto University. The calcined *Sample* was placed in a Teflon sample holder. The spectra were measured at 9-12 K. The γ-ray source was [197]Pt prepared by neutron irradiation to [196]Pt (half-life: 18.6 h, γ-ray energy: 77.4 keV). The spectra were analyzed using a computer software by assuming that each spectrum consists of Lorentzian function.

IV-3   Results and discussion

IV-3-1   XRD

The XRD patterns of the calcined *Sample* and the standards (metal Cu and Au) are displayed in Fig. IV-1.   The XRD pattern for the calcined *Sample* showed the four strong diffraction peaks at 2θ=38.84 °, 45.24 °, 65.62 ° and 79.00 °.   Each diffraction peak for the calcined *Sample* appeared between the corresponding peaks of the (111), (200), (220) and (311) crystal faces of Au and Cu, suggesting that the calcined *Sample* may be a Au-Cu alloy. According to Vegard's law [44], each diffraction face of the Au-Cu alloy phase can be observed between the corresponding diffraction faces of both Au and Cu.   Thus, this phase was ascribed to an Au-Cu alloy with a single phase, although a small peak was observed at approximately 40 °, suggesting that another alloy phase may have formed slightly.

IV-3-2   XAS and in-situ XAS

Figure IV-2 shows the Cu K-edge XANES spectra for $Cu(OH)_2$ (a) as a standard of Cu (II), Au_5Cu_5 alloy (b) as a standard of Au-Cu alloy, the calcined *Sample* (c) and Cu foil (d) as a standard of Cu (0).   The Cu K-edge XANES spectrum for the calcined *Sample* did not show a white line at 8.99 keV which indicates an ionic character, suggesting that the Cu in the calcined *Sample* is concluded to be present as Cu (0).   However, the XANES spectrum for the calcined *Sample* was significantly different from that of Cu foil.   The XANES spectrum for the calcined *Sample* was shifted to low-energy side compared with that of Cu foil and was rather similar to that for the Au_5Cu_5 alloy.   The fact suggests that the chemical state of Cu (0) in the calcined *Sample* may be different from that in Cu foil.   Figure IV-3 shows the Fourier transform of EXAFS oscillation Cu K-edge spectra for $Cu(OH)_2$ (a), Au_5Cu_5 alloy (b), the calcined *Sample* (c) and Cu foil (d).   In Fig. IV-3, the shape of the spectrum for the calcined *Sample* was very

similar to that for Au₅Cu₅ alloy.   Figure IV-4 shows the Au L_3-edge XANES spectra for

Au(OH)$_3$ (a) as a standard of Au (III), Au$_5$Cu$_5$ alloy (b) as a standard of Au-Cu alloy, the

calcined *Sample* (c) and Au foil (d) as a standard of Au (0).   Interestingly, the Au L_3-edge

XANES spectrum for the calcined *Sample* showed no white line at 11.92 keV in contrast with

that for Au(OH)$_3$.   Furthermore, the shape of the XANES spectrum of the calcined *Sample* was

significantly different from that of Au foil.   On the other hand, the spectrum was similar to the

shape of the XANES spectrum for the Au$_5$Cu$_5$ alloy.   These facts suggest that the chemical

state of Au (0) in the calcined *Sample* may be different from that in Au foil.   Figure IV-5 shows

the Fourier transform of EXAFS oscillation Au L_3-edge spectra for Au(OH)$_3$ (a), Au$_5$Cu$_5$ alloy

(b), the calcined *Sample* (c) and Au foil (d).   In Fig. IV-5, the first peak in the spectra for Au

foil and Au(OH)$_3$ corresponds in principle to the Au-Au and Au-O interactions, respectively.

The distance of Au-Au interaction is longer than that of Au-O interaction based on the atomic

radii of Au and O atoms.   The peak of the calcined *Sample* was slightly shorter in distance

compared with the distance of Au-Au interaction, suggesting that neighboring atoms exist at

different distance from the distance of Au-Au interaction of Au foil and that of Au-O interaction

of Au(OH)$_3$ in case of the calcined *Sample*.   The results of both Cu K-edge and Au L_3-edge

XAS measurements for the calcined *Sample* indicated that a new phase with Au-Cu interaction

formed.

In order to observe the change in the chemical state of Cu in the precursor during the

calcination under hydrogen gas flow, *in-situ* Cu K-edge XANES spectra for the precursor were

measured in the temperature range from RT to 573 K.   The results of the *in-situ* Cu K-edge

XANES spectra are shown in Fig. IV-6.   The intensity of white line at 8.99 keV gradually

decreased with the calcination temperature of the precursor, and the white line disappeared at

448 K, suggesting that almost all of the Cu(OH)$_2$ in the precursor was reduced at 448 K.

Fourier transforms of *in-situ* EXAFS oscillation Cu K-edge spectra during the calcination of the

precursor are shown in Fig. IV-7.   The peak at 1.2 Å can be assigned to Cu-O interaction, and

the peak at 2.2 Å can be assigned to Cu-Au interaction from the comparison between spectra for

the Au_5Cu_5 alloy (Fig. IV-3) and the precursor calcined above 448 K.   Similar to the change in

the *in-situ* Cu K-edge XANES spectra, the peak due to Cu-O interaction was observed below

448 K, and the peak due to Cu-Au interaction appeared above 448 K.   The results of the *in-situ*

Au L_3-edge XANES spectra for the precursor under hydrogen gas flow at RT-573 K and the

standards are shown in Fig. IV-8.   The intensity of white line at 11.92 keV decreased with

increasing temperature to 398 K, suggesting that the $Au(OH)_3$ in the precursor is reduced until

398 K.   Fourier transforms of *in-situ* EXAFS oscillation Au L_3-edge spectra for the calcined

Sample are shown in Fig. IV-9.   The peak at 1.5 Å can be assigned to Au-O interaction, and the

peak at 2.5 Å can be assigned to Au-Cu interaction from the comparison between spectra for the

Au_5Cu_5 alloy (Fig. IV-5) and the precursor calcined above 398 K.   Similar to the change in the

in-situ Au L_3-edge XANES spectra, the peak due to Au-O interaction was observed below 398

K, and the peak due to Au-Cu interaction appeared above 398 K.   The above results revealed

that $Au(OH)_3$ in the precursor was reduced at lower temperature compared with the reduction

temperature of $Cu(OH)_2$, and then the Au-Cu powder alloy was formed by solution of Cu atoms

into metal Au through the reduction of $Cu(OH)_2$ to Cu atom.   This formation mechanism of

Au-Cu alloy was supported by the appearance of the peak due to Au-Cu interaction in the

precursor at 398 K.   The peak shifted to shorter distance with increasing temperature to 573 K

which is the calcination temperature, suggesting that the mixing of Au(0) and Cu(0) may

proceed more effectively.

IV-3-3 ^{197}Au Mössbauer spectroscopy

In order to obtain the detailed information on the chemical state of Au included in the

calcined *Sample*, ^{197}Au Mössbauer spectra were measured.   In ^{197}Au Mössbauer spectroscopy,

the different chemical states of Au can be separately detected depending on the isomer shift (IS)

and the quadrupole splitting (QS).   Figure IV-10 shows the ^{197}Au Mössbauer spectra for

$Au(OH)_3$ (a) as a standard of Au (III), the calcined *Sample* (b) and Au foil (c) as a standard of

Au (0).   It was difficult to measure the spectrum for the Au_5Cu_5 alloy because of its hardness. Despite the fact that the Au in the calcined *Sample* was assigned to Au (0) in the Au L_3-edge XANES spectra in Figs. IV-4 and IV-8, the ^{197}Au Mössbauer spectrum for the calcined *Sample* was different from that of Au foil.   The spectrum for the calcined *Sample* clearly showed a peak with positive isomer shift, suggesting that the Au (0) in the calcined *Sample* is present in a specific Au (0) state with Au (0)-Cu (0) bonds accompanying the transfer of slight electron density from Au (0) to Cu (0).   The ^{197}Au Mössbauer parameters are tabulated in Table IV-1. According to the literature [45], the ^{197}Au Mössbauer spectrum for the $AuCu_3$ intermetallic alloy showed one peak with a positive isomer shift as shown in Table IV-1.   As a result, the Au in the calcined *Sample* could be assigned to Au (0) with the Au-Cu interaction as shown in Fig. IV-5. The IS value for the calcined *Sample* was small compared with that of the previous study as shown in Table IV-1.   The IS value is known to be sensitive to the electron density around Au atomic nucleus in the sample.   Therefore, the above result was attributed to the fact that the strength of Au-Cu interaction in the calcined *Sample* was different from that of $AuCu_3$ intermetallic alloy.   In short, it can be reasonably concluded that the calcined *Sample* was an Au-Cu alloy other than $AuCu_3$ intermetallic alloy.

The Au-Cu alloy was considered to be formed by the following mechanism.   First, $Au(OH)_3$ in the precursor, which is a mechanical mixture of $Au(OH)_3$ and $Cu(OH)_2$, was reduced to Au (0) by thermal decomposition reaction at approximately 398 K.   Then, hydrogen atoms with a strong reduction ability were generated by dissociative adsorption on the Au (0) (Au nanoparticles)[35].   Next, the hydrogen atom reduced $Cu(OH)_2$ in the precursor to Cu (0) at approximately 448 K.   Then, Au (0) and Cu (0) were mixed at the atomic level, and the Au-Cu alloy consisting of a single phase was formed.
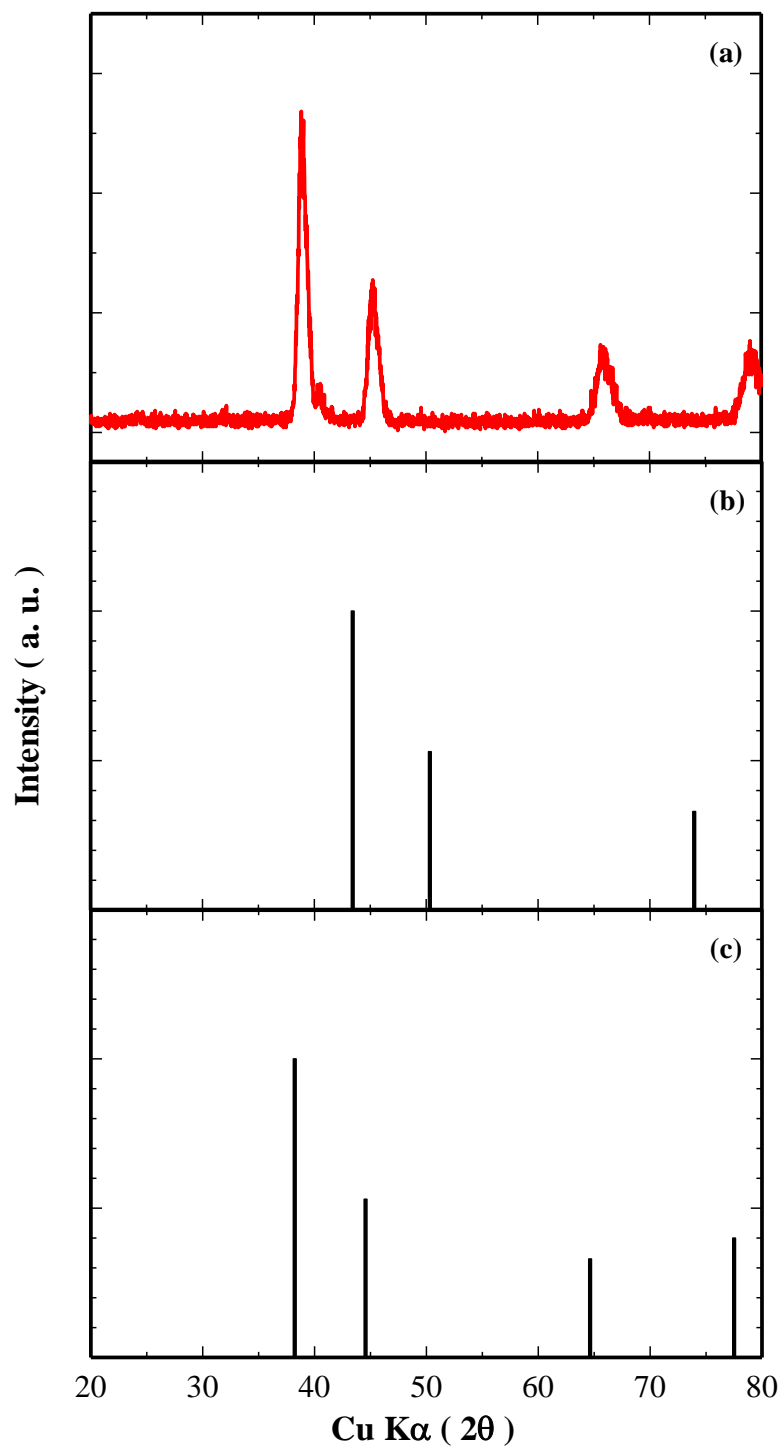
Fig. IV-1   XRD patterns of the calcined *Sample* (a), Cu (ICDD: 00-001-1424) (b)

and Au (ICDD: 00-001-1172) (c).

The diffractograms for Cu and Au were given from data base (ICDD).
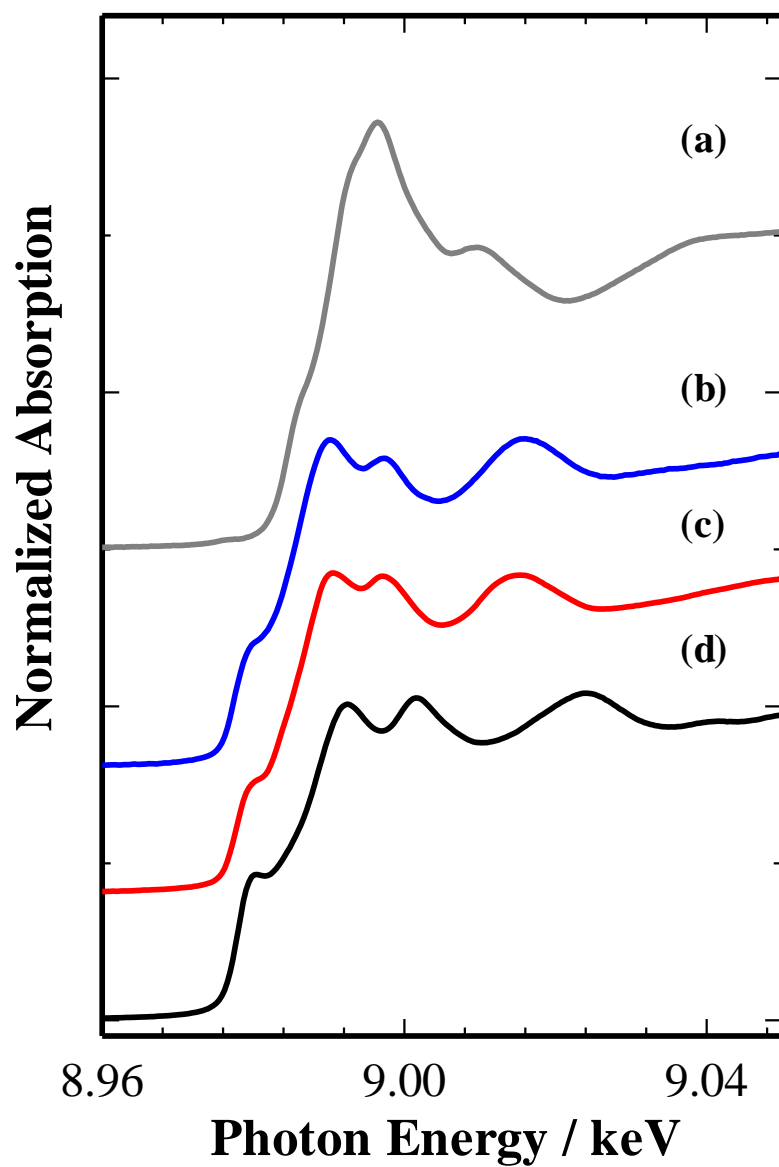
Fig. IV-2   Normalized Cu K-edge XANES spectra for $Cu(OH)_2$ (a),

Au_5Cu_5 alloy (b), the calcined *Sample* (c) and Cu foil (d).

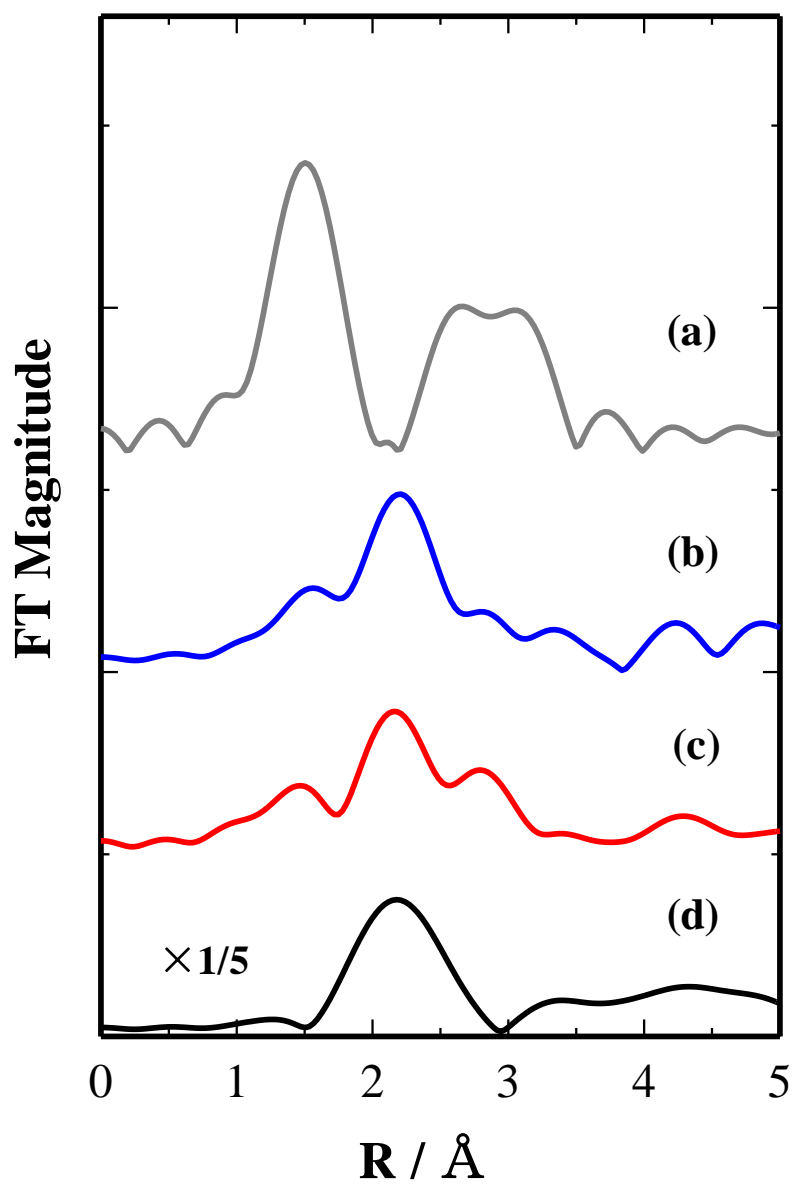Fig. IV-3   Fourier transform of EXAFS oscillation Cu K-edge spectra for Cu(OH)$_2$ (a),

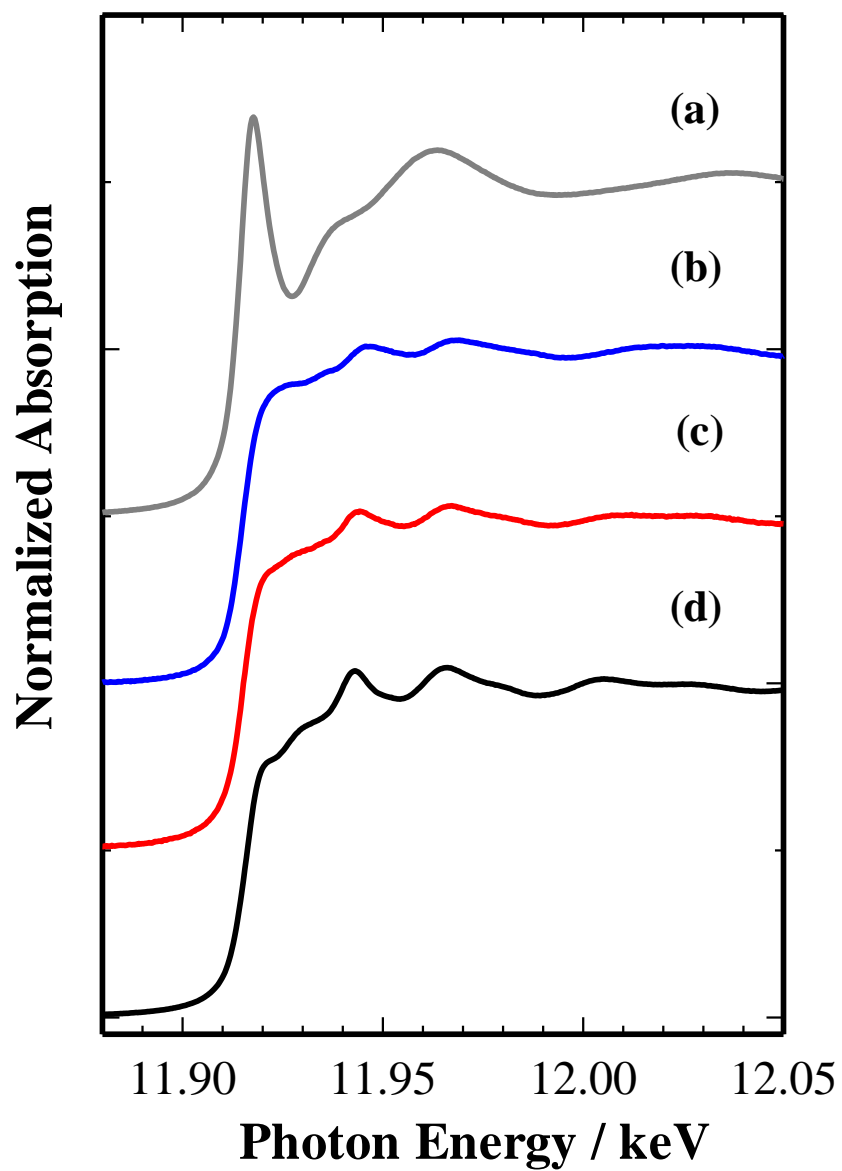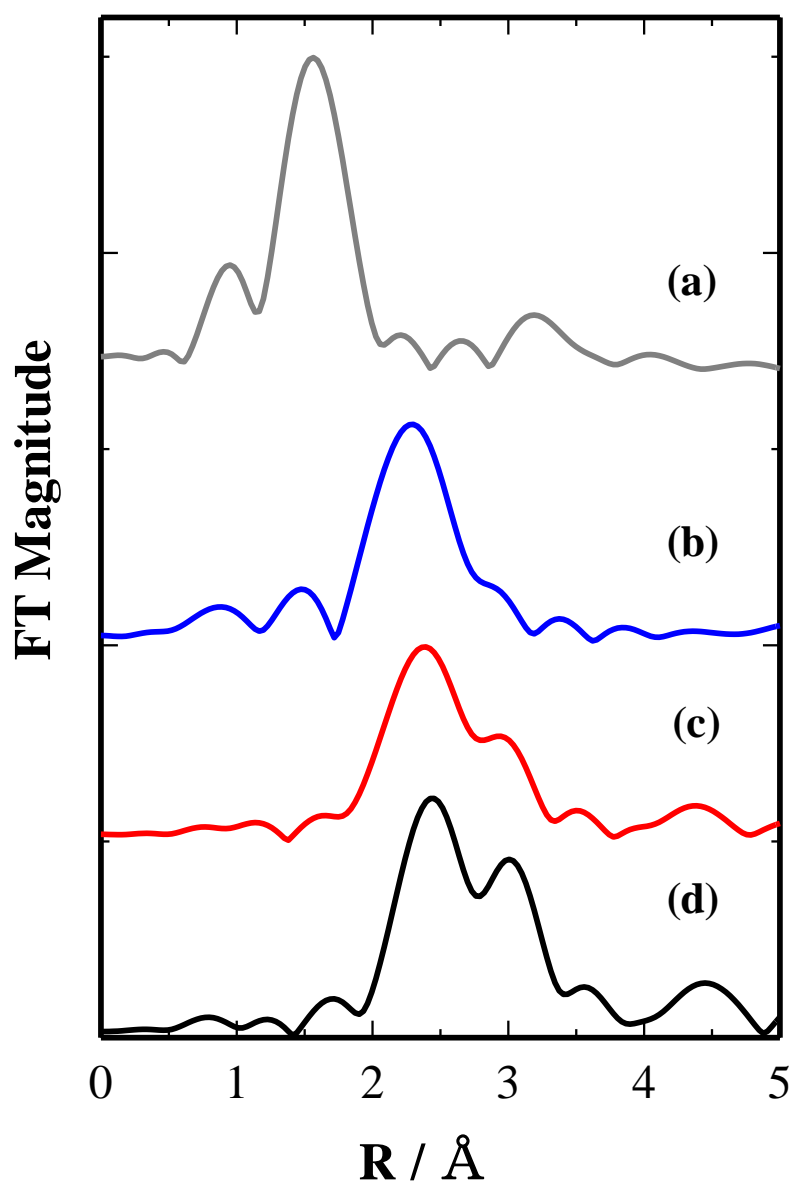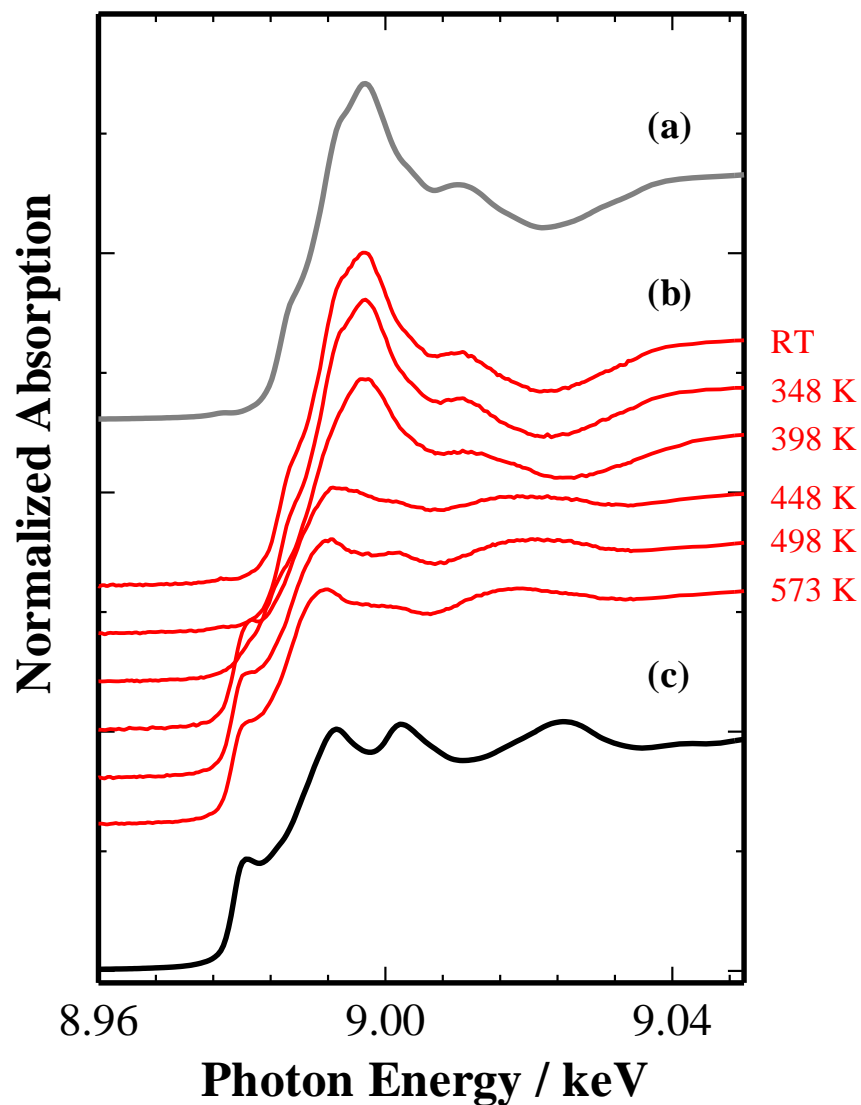Au$_5$Cu$_5$ alloy (b), the calcined *Sample* (c) and Cu foil (d).

Fig. IV-4   Normalized Au L_3-edge XANES spectra for $Au(OH)_3$ (a), Au_5Cu_5 alloy (b),

the calcined *Sample* (c) and Au foil (d).

Fig. IV-5   Fourier transform of EXAFS oscillation Au L_3-edge spectra for $Au(OH)_3$ (a),

Au_5Cu_5 alloy (b), the calcined *Sample* (c) and Au foil (d).

Fig. IV-6 Normalized *in-situ* Cu K-edge XANES spectra for $Cu(OH)_2$ (a), the calcined

precursor (the numbers in the figure mean Kelvin absolute temperature) (b) and Cu foil (c).

Spectra (a) and (c) were measured at RT.

Spectra (b) were measured at each temperature shown in the figure.

Calcination temperature: RT-573 K.

Atmosphere: under hydrogen gas flow.

Fig. IV-7   Fourier transform of *in-situ* EXAFS oscillation Cu K-edge spectra

for Cu(OH)$_2$ (a), the calcined precursor (b) and Cu foil (c).

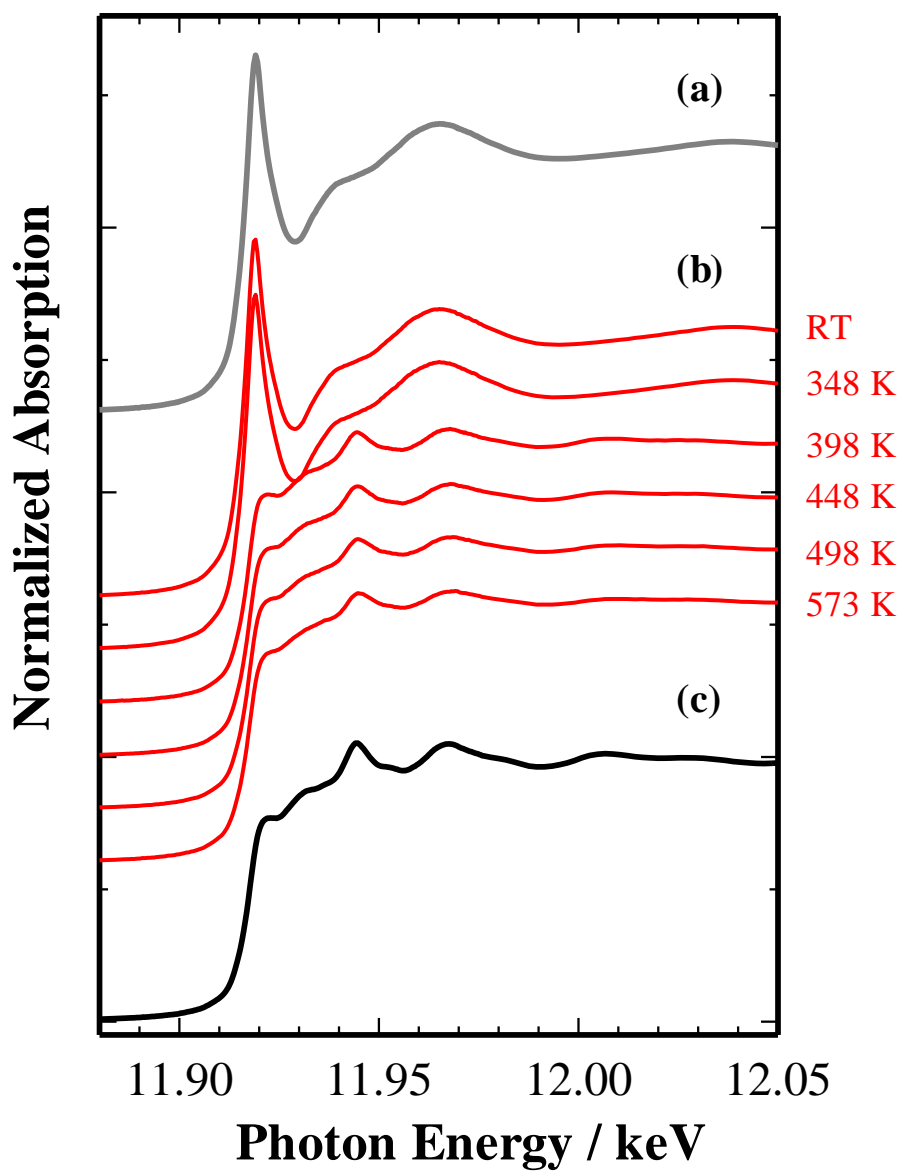Each peak in this figure corresponds to that in Fig. IV-6.
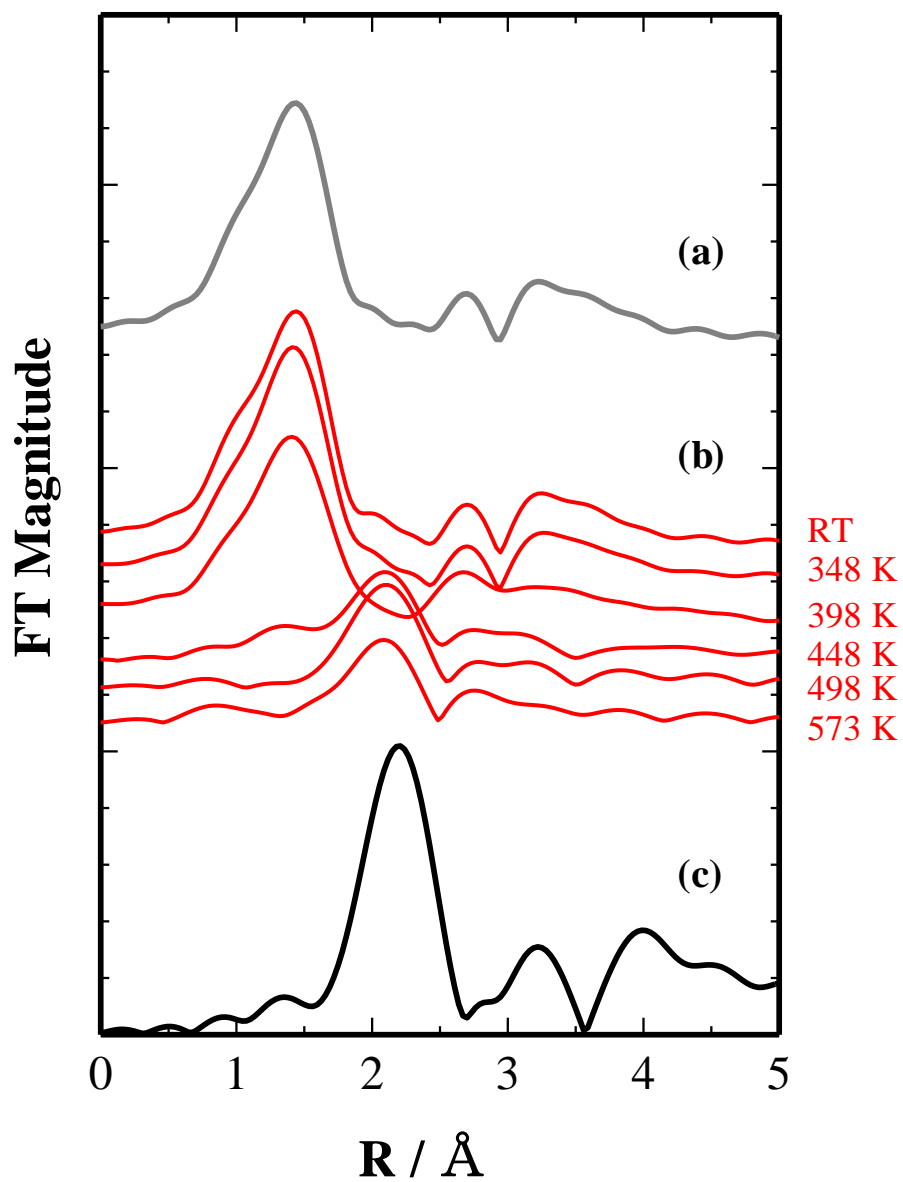
Fig. IV-7   Fourier transform of *in-situ* EXAFS oscillation Cu K-edge spectra

for Cu(OH)$_2$ (a), the calcined precursor (b) and Cu foil (c).

Each peak in this figure corresponds to that in Fig. IV-6.

Fig. IV-8 Normalized *in-situ* Au L_3-edge XANES spectra for $Au(OH)_3$ (a), the calcined

precursor (the numbers in the figure mean Kelvin absolute temperature) (b) and Au foil (c).

Spectra (a) and (c) were measured at RT.

Spectra (b) were measured at each temperature shown in the figure.

Calcination temperature: RT-573 K.
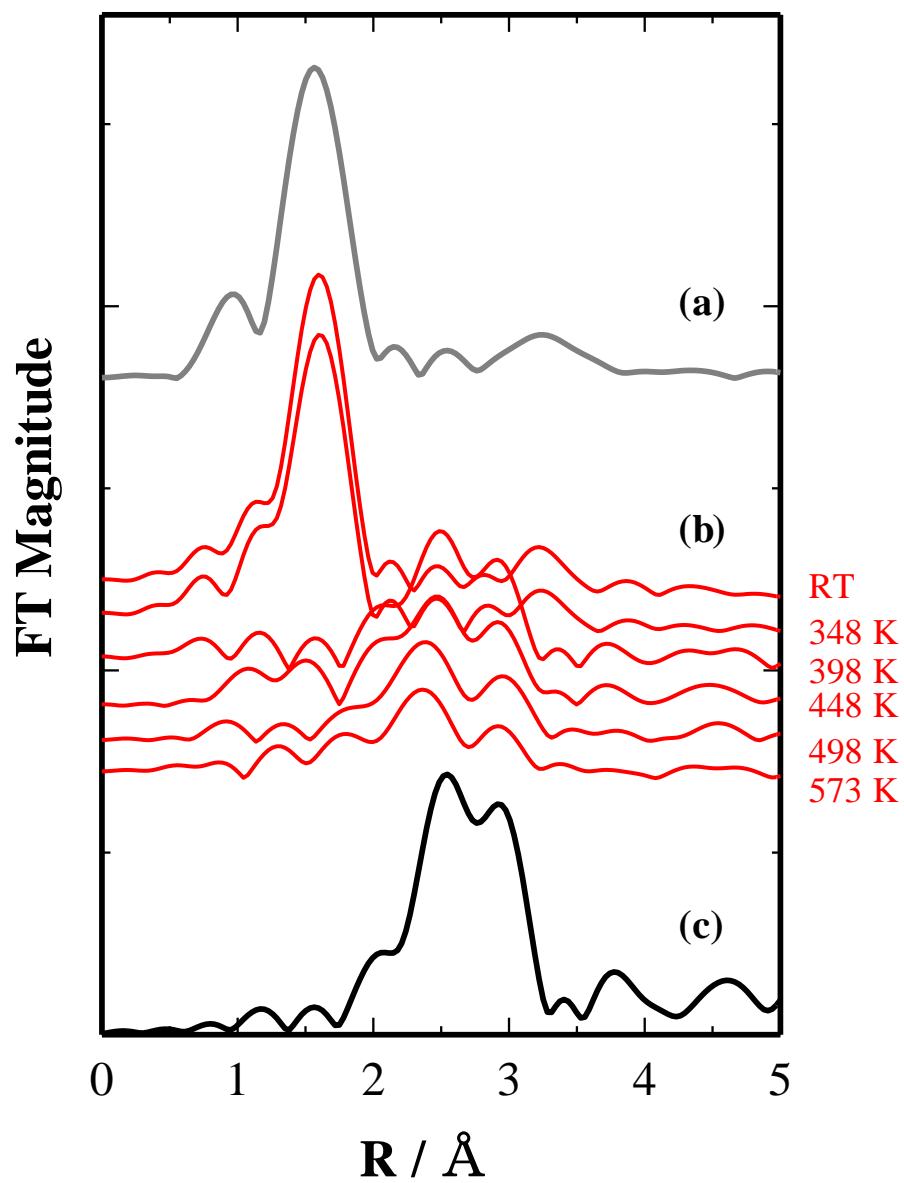
Atmosphere: under hydrogen gas flow.

Fig. IV-9   Fourier transform of *in-situ* EXAFS oscillation Au L$_3$-edge spectra

for Au(OH)$_3$ (a), the calcined precursor (b) and Au foil (c).

Each peak in this figure corresponds to that in Fig. IV-8.

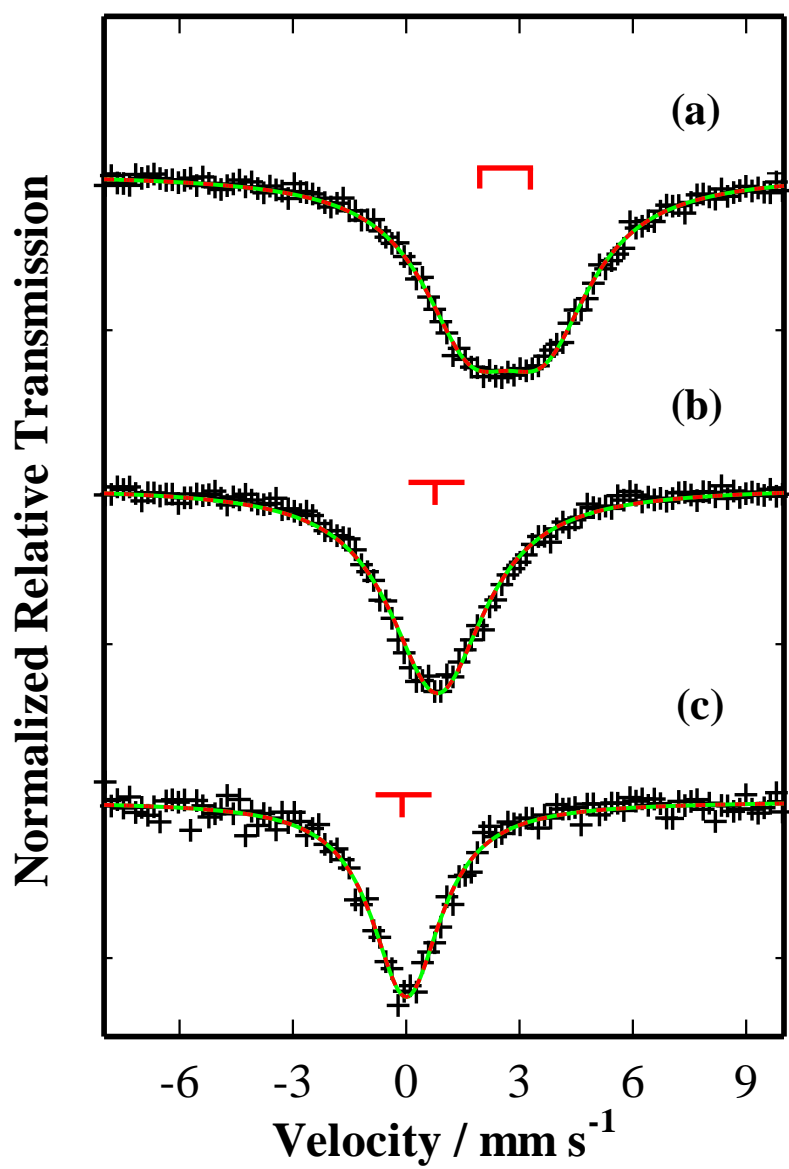Fig. IV-10   [197]Au Mössbauer spectra for Au(OH)$_3$ (a), the calcined *Sample* (b)

and Au foil (c).

Table IV-1   [197]Au Mössbauer parameters for the standards and the calcined *Sample*.

Sample name	Mössbauer parameters	
	IS / mm s^{-1}	QS / mm s^{-1}
Au foil	0.00±0.02	-
Au(OH)$_3$	2.67±0.03	1.98±0.03
the calcined *Sample*	0.82±0.01	-
AuCu$_3$ intermetallic alloy [45]	3.55	-

Chapter V

Conclusion

From the results of the investigation of the change in electronic state of the hydrolysis of tetrachloroaurate ion ($[AuCl_4]^-$) using the relativistic version of DV-$X\alpha$ method, revealed the following. From the net charge obtained, it is concluded that the ionic property of Au increased as hydrolysis proceeds. Especially, when $[AuCl_4]^-$ transforms to $[AuCl_3(OH)]^-$, the change in the net charge of Au was largest compared with other transformations. Therefore, it was revealed that the electronic state changes most greatly at the first step of hydrolysis. From the values of the bond overlap population, Au-Cl and Au-O interaction were concluded to be single bond. Moreover, it was revealed that the Au-Cl interaction had stronger affinity than the Au-O interaction. The theoretical Au L_3-edge XANES spectra for $[AuCl_4]^-$ and $[Au(OH)_4]^-$ obtained from the DV-$X\alpha$ calculation were agree well to both of Au L_3-edge XANES spectra for $[AuCl_4]^-$ and $[Au(OH)_4]^-$ observed, indicating that these calculation results were reasonable and proper.

From the results of the investigation of the chemical and physical properties of gold (III) hydroxide, revealed the following. The size and morphology of the obtained gold (III) hydroxide were 8.83±3.47 nm and X-ray amorphous. From the results of the curve fitting analysis of the EXAFS and the weight loss observed by TG measurement, the chemical composition of the gold (III) hydroxide could be concluded $Au(OH)_3$. From the result of ATR-IR spectroscopy, the absorption assigned to Au-O interaction was observed at 575 cm^{-1}. The UV-Vis spectrum for the gold (III) hydroxide did not show the discriminative peak. The thermal decomposition reactions under a flow of air and hydrogen gas were investigated. Under a flow of air, the thermal decomposition reaction of $Au(OH)_3$ was demonstrated to be 2 step reactions from the results of TG/DTA measurement, O_2-TPR profile and detection of O_2 and H_2O generated during the reaction by the quadrupole mass spectroscopy. Under a flow of hydrogen gas, the thermal decomposition reaction of $Au(OH)_3$ was also demonstrated to be 2

step reactions from the results of H_2 flow *in-situ* XAS, H_2-TPR profile and the detection of H_2 consumed and H_2O generated during the reaction by the quadrupole mass spectroscopy.

Furthermore, the solubility of $Au(OH)_3$ measured from both sides of supersaturation and of undersaturation.   As a result, the solubility of $Au(OH)_3$ at 297 K was determined to be 0.00131 g/100 g of H_2O.

From the results of a novel preparation method of a single phase Au-Cu powder alloy and its characterization, an Au-Cu powder alloy consisting of a single phase was successfully prepared.   In the preparation a mixture of $Cu(OH)_2$ and $Au(OH)_3$ was calcined under hydrogen gas flow at 573 K.   The advantage of this method is that an Au-Cu powder alloy can be prepared at a relatively low temperature.   In addition, it is easy to control the composition of the Au-Cu alloy because of the accurate weighing of $Cu(OH)_2$ and $Au(OH)_3$.   This method may be applied to the preparation of Au-M powder alloys containing metal elements other than Cu.

Acknowledgements

Reference

[1]   D. Vlassopoulos and S. A. Wood, *Geochim. Cosmochim. Acta,* **54** (1990) 3-12.

[2]   P. J. Renders and T. M. Seward, *Geochim. Cosmochim. Acta,* **53** (1989) 245-253.

[3]   J. G. Webster, *Geochim. Cosmochim. Acta,* **50** (1986) 1837-1845.

[4]   A. W. Mann, *Econ. Geol.,* **79** (1984) 38-49.

[5]   W. E. Baker, *Geochim. Cosmochim. Acta,* **42** (1978) 645-649.

[6]   H. W. Lakin, G. C. Curtin, A. E. Hubert, H. T. Scacklette and K. G. Doxtader, *USGS Bull* **1330** (1974).

[7]   H. L. Ong and V. E. Seanson, *Q. Colo. Sch. Mines,* **64** (1969) 395-425.

[8]   M. Haruta, N. Yamada, T. Kobayashi and S. Iijima, *J. Catal.,* **115** (1989) 301-309.

[9]   Y. Kobayashi, S. Nasu, S. Tsubota and M. Haruta, *Hyperfine Interact.,* **126** (2000) 95-99.

[10]   K. Okumura, K. Yoshino, K. Kato, M. Niwa, *J. Phys. Chem. B*, **109** (2005) 12380-12386.

[11]   J. A. Peck, C. D. Tait, B. I. Swanson and G. E. Brown Jr., *Geochim. Cosmochim. Acta,* **55** (1991) 671-676.

[12]   P. J. Murphy and M. S. Lagrange, *Geochim. Cosmochim. Acta,* **62** (1998) 3515-3526.

[13]   M. L. Machesky, W. O. Andrade and A. W. Rose, *Geochim. Cosmochim. Acta,* **55** (1991) 769-776.

[14]   A. Uchida, T. Yokoyama, Y. Motomura, A. Miyazaki, Y. Okaue, K. Watanabe and E. Izawa, *Resource Geology*, **52** (2002) 223-230.

[15]   B. Ravel and M. Newville, *J. Synchrotron Rad.,* **12** (2005) 537-541.

[16]   M. Bonamico and G. Dessy, *Acta Cryst.,* B29 (1973) 1735-1736.

[17]   C. Lee, W. Yang and R. G. Parr, *Phys. Rev. B,* **37** (1988) 785-789.

[18]   A. D. Becke, *J. Chem. Phys.,* **98** (1993) 5648-5652.

[19]   A. Rosén, D. E. Ellis, H. Adachi and F. W. Averill, *J. Chem. Phys.,* **65** (1976) 3629-3634.

[20]   H. Adachi, M. Tsukada and C. Satoko, *J. Phys. Soc. Jpn.,* **45** (1978) 875-883.

[21]   J. C. Slater, *Phys. Rev.,* **81** (1951) 385-390.

[22]   J. C. Slater, The Calculation of Molecular Orbitals (John Wiley & Sons, New York, 1979) Chap. 2.

[23]   M. Pepper and B. E. Bursten, *Chem. Rev.,* **91** (1991) 719-741.

[24]   P. Pyykkö, *Chem. Rev.,* **88** (1988) 563-694.

[25]   H. Nishikawa, D. Kawamoto, Y. Yamamoto, T. Ishida, H. Ohashi, T. Akita, T. Honma, H. Oji, Y. Kobayashi, A. Hamasaki, T. Yokoyama and M. Tokunaga, *J. Catal.,* **307** (2013) 254-264.

[26]   B. S. Uphade, S. Tsubota, T. Hayashi and M. Haruta, *Chem. Lett.,* **27** (1998) 1277-1278.

[27]   H. L. Johnston and H. L. Leland, *J. Am. Chem. Soc.,* **60** (1938) 1439-1445.

[28]   H. Schütza and I. Schütza, Z. Anorg. Allg. Chem., **245** (1940) 59-66.

[29]   P. V. Parish, in: Mössbauer Spectroscopy Applied to Inorganic Chemistry, Vol. 1, ed. G. J. Long (Plenum, New York, 1984) p. 21

[30]   X. Chen, W. Chu, D. Chen, Z. Wu, A. Marcelli and Z. Wu, *Chem. Geol.,* **268** (2009) 74-80.

[31]   M. Hisamoto and S. L. Scott, *Spectrochim. Acta, Part A,* **71** (2008) 969-974.

[32]   S. Link, C. Burda, M. B. Mohamed, B. Nikoobakht and M. A. El, *J. Phys. Chem. A,* **103** (1999) 1165-1170.

[33]   D. Kawamoto, H. Nishikawa, H. Ohashi, H. Oji, T. Honma, Y. Kobayashi, A. Hamasaki, T. Ishida, Y. Okaue, M. Tokunaga and T. Yokoyama, *Adv. X-ray Chem. Anal. Japan,* **43** (2012) 293-302.

[34]   M. Piccinini, E. Ntainjua N., J. K. Edwards, A. F. Carley, J. A. Mouliji and G. J. Hutchings, *PCCP,* **12** (2010) 2488-2492.

[35]   T. Fujitani, I. Nakamura, T. Akita, M. Okumura and M. Haruta, *Angew. Chem. Int. Ed.,* **48** (2009) 9515-9518.

[36]   S. Link, Z. L. Wang and M. A. El, *J. Phys. Chem. B,* **103** (1999) 3529-3533.

[37]   N. Toshima, M. Harada, T.Yonezawa, K. Kushihashi and K. Asakura, *J. Phys. Chem.,* **95** (1991) 7448-7453.

[38]   M. T. Reetz, W. Helbig and S. A. Quaiser, *Chem. Mater,* **7** (1995) 2227-2228.

[39]   M. A. Bratescu, O. Takai and N. Saito, *J. Alloys Compd.,* **562** (2013) 74-83.

[40]   M. Khoudiakov, M. C. Gupta and S. Deevi, *Appl. Catal. A,* **291** (2005) 151-161.

[41]   S. Kameoka and A. P. Tsai, *Catal. Lett.,* **121** (2008) 337-341.

[42]   X. Liao, W. Chu, X. Dai and V. Pitchon, Appl. Catal. B, **142-143** (2013) 25-37.

[43]   J. P. Nielsen and J. J. Tuccillo, *J. Dent. Res.,* **45** (1966) 964-969.

[44]   L. Vegard, *Zeitschrift für Physik,* **5** (1921) 17-26.

[45]   D. J. Erickson and L. D. Roberts, *Phys. Rev. B,* **9** (1974) 3650-3657.